Molecular mechanism of mechanical breathing in organic mixed ionic-electronic conductors

Xixian Yang[†], Hong Sun[†,‡], Xiaomei He[†], Kejie Zhao[†,*]

[†]School of Mechanical Engineering, Purdue University, West Lafayette, IN 47907, United States

[‡]Physics Division, Lawrence Livermore National Laboratory, Livermore, CA 94550, United States

Table of Contents Graphic

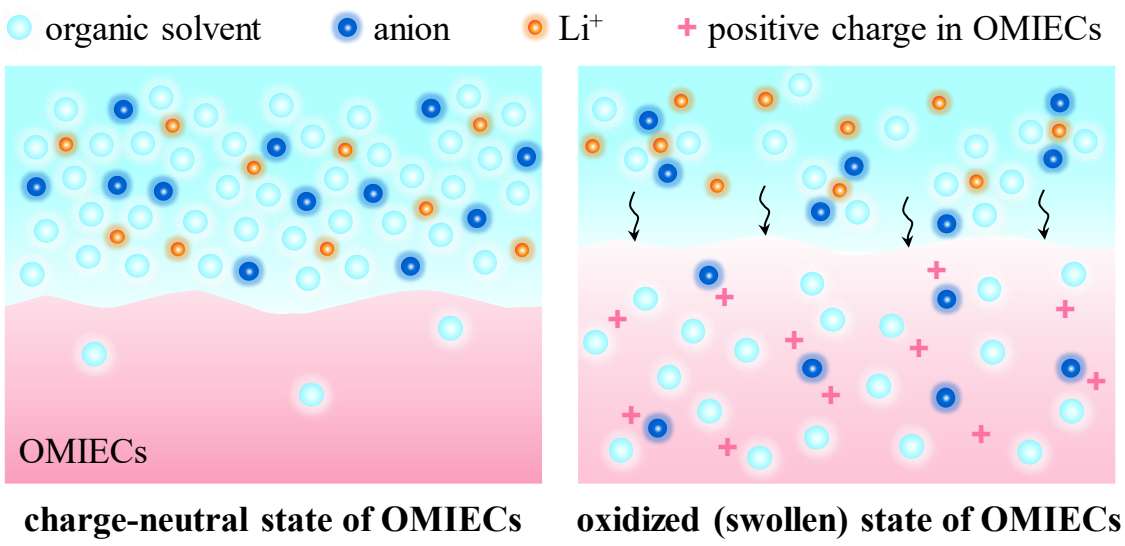

ABSTRACT

Mechanical breathing of organic mixed ionic-electronic conductors (OMIECs) is a structural response upon redox reactions. The breathing strain is often in the range of a few percentages to a few hundred percentages in different OMIECs operated in different chemical environments. Such mechanical activation needs to be tailored such as to be maximized in actuators and to be minimized in increasing the device reliability. We perform atomistic modeling to understand the molecular mechanism of mechanical swelling of OMIECs immersed in various electrolytes and at different oxidation states. We study poly(3,4-propylenedioxythiophene) (PProDOT) which is widely used in organic electrochromic devices as a model system and compare its swelling behavior in electrolytes of different salt concentrations, solvents, and anions. PProDOT deforms more in the electrolyte of a lower salt concentration and larger anions. Mass transport of the electrolyte, especially the organic solvent, is dominant in regulating mechanical swelling of PProDOT compared to the electrostatic interactions. We examine the evolution of the microstructural features and local bonding environments associated with the mixed conduction upon oxidation. We calculate the diffusion coefficients of the cation, anions, and solvents in the mixture of PProDOT and the electrolyte, which inform the swelling kinetics of PProDOT and the solvation structure in the electrolyte. The results are further validated by different self-aggregated PProDOT configurations and modeling protocols. The finding is in good agreement with the experiments and provides fundamental understanding of the molecular motifs underpinning the breathing strain in OMIECs.

*Corresponding author (Email: kjzhao@purdue.edu)

Introduction

Organic mixed ionic-electronic conductors (OMIECs) are now widely explored in organic electrochromic devices (OECDs),[1–3] organic electrochemical transistors (OECTs),[4–6] energy storage devices,[7,8] biomedical sensors,[9,10] and dynamic microfiltration systems[11,12] due to their key feature of mixed conduction of ions and electrons/holes. Compared to the inorganic counterpart, organic mixed conductors have the advantages of material versatility, flexibility in synthesis, biocompatibility, and low cost,[4,13–15] and therefore they have attracted intensive interest in recent years. In OMIECs, electrons and holes are conducted in the polymer network with concurrent injection of counterions from the electrolyte to maintain the charge neutrality. This process is also often associated with absorption of the solvent into the OMIECs.[16,17] Polymers respond to the injected charge carriers and solvent by rearranging the chain microstructure.[18,19] Likewise, the conduction process is reversed when a backward sweep of voltage is applied. This cyclic process is accompanied by injection and ejection of compensating charge carriers and solvent. OMIECs respond to the mass transport and local electrostatic interactions of charged species by mechanical breathing – a macroscopic and repetitive volume change in the course of doping and dedoping processes.[20,21] The breathing strain can be utilized for actuation[22–24] or microfiltration,[11,12] in which the mechanical swelling is desired to be maximized for a large range of motion or a broad size selectivity. Nevertheless, when OMIECs are integrated into devices such as OECDs, they are often bonded on top of a current-collector substrate which is mechanically inactive.[25,26] Mechanical activation of the polymer induces mismatch between the OMIECs film and the substrate and causes large stresses at the interface, which result in a variety of mechanical damage such as channel cracks, wrinkling, and delamination of OMIECs.[20,27] The mechanical disintegration disrupts charge conduction across the interface between the film and the substrate and significantly

compromises the reliability and durability of OMIECs-based devices. In this application, mechanical breathing is a detrimental factor and is desired to be minimized. Besides, electrolyte infiltration brings about irreversible morphological changes of OMIECs, and further changes the charge transport properties. For instance, in OECTs, moderate electrolyte uptake and associated strain activation are required for a high transconductance and a fast-switching speed.[28,29] Therefore, mechanical swelling of OMIECs in such applications needs to be optimized. Overall, mechanical breathing is a structural response to the redox reactions in OMIECs and its amplitude should be carefully tailored in the respective applications to achieve enhanced performance and prolonged operational lifespan.

Previous studies suggested multiple strategies to tailor the mechanical breathing of OMIECs used for actuators, microfilters, and OECTs in aqueous environment, including adjusting the film thickness,[18,21] heat treatment,[30] and side chain engineering.[3,31,32] For instance, swapping the alkyl side chain by the hydrophilic ethylene glycol side chain can boost water uptake of OMIECs.[33,34] Besides, tuning the side chain length allows for different degrees of mechanical swelling.[12] Notably, the mechanical response of OMIECs is dependent on the choice of the electrolyte. Hara et al. found that the electrochemical strain of polypyrrole (PPy) is positively correlated to the size of anions (PF_6^- > BF_4^- > Cl^-) in the electrolyte for conducting polymer actuators.[22] Savva et al. measured the swelling volume of poly(2-(3,3'-bis(2-(2-(2-methoxyethoxy)ethoxy)ethoxy)-[2,2'-bithiophen]-5-yl)thieno[3,2-b] thiophene) (p(g2T-TT)) OECTs in NaCl aqueous solution via electrochemical quartz crystal microbalance with dissipation monitoring (EQCM-D), and observed a larger mechanical swelling of p(g2T-TT) in the electrolyte of lower salt concentrations due to the larger hydration shell of Cl^-.[28] Similar dependence of mechanical swelling on anion hydration was reported in other studies.[35]

Despite the importance of mechanical activation in OMIECs, theoretical understanding of the breathing strain in response to the mass transport and local electrostatic interactions in the polymer network remains limited. More specifically, there have been few systematic studies on mechanical breathing of OMIECs in different organic electrolytes.[21] Different from aqueous electrolytes where anions hydrated with water diffuse into the polymer, in organic electrolytes such as lithium salt electrolytes, Li ions are dissociated by the organic solvent at the electrolyte-polymer interface whilst anions are injected into (p-type) OMIECs. We measured breathing strains of poly(3,4-propylenedioxythiophene) (PProDOT) immersed in a variety of organic electrolytes using in-situ nanoindentation experiments.[20,21] We found that the swelling strain is in the range of 12%-25% depending on the specific salt concentrations, organic solvents, and anions. In this work, we conduct theoretical modeling using all-atom molecular dynamics (MD) simulations to understand the molecular mechanism of mechanical breathing in OMIECs at different oxidation states and in different electrolyte environments. We use poly(3,3-bis(2-ethylhexyloxymethyl)-3,4-dihydro-2H-thieno[3,4-b][1,4]dioxepine) (PProDOT-$(OEtHx)_2$), which is widely used in OECDs, as a model system (for simplicity, PProDOT-$(OEtHx)_2$ will be referred to as PProDOT hereafter, similarly, ProDOT-$(OEtHx)_2$ will be referred to as ProDOT). We construct the PProDOT molecular structure and analyze its structural features at the dry pristine state as the reference. Upon doping within a given organic electrolyte, we measure the swelling volume of PProDOT and evaluate the evolution of the chain microstructure. We differentiate the contributions of mass transport and electrostatic interactions to the overall strain actuation. We then focus on the interactions between PProDOT and the electrolyte of different anions, salt concentrations, and organic solvents. We compare the swelling behaviors of PProDOT soaked in 0.2 molar (M) and 1.0 M $LiClO_4$ in propylene carbonate (PC), 1.0 M $LiBF_4$, $LiPF_6$, and LiTFSI in PC, and 1.0 M

$LiPF_6$ in ethylene carbonate/diethyl carbonate (EC/DEC). The influence of the salt molarity, organic solvent, and anion is evaluated through the swelling volume measurement and evolution of the morphological characteristics and local bonding environment of the polymer network. We further determine the diffusion coefficients of the cation, anions, and solvents in the mixture of PProDOT and the electrolyte, which inform the swelling kinetics of PProDOT and the solvation structure in the electrolyte. The modeling results of mechanical swelling of PProDOT and the transport properties of the electrolyte are placed in parallel with our prior experimental measurements, and they find good agreement. In addition, the results are validated using different self-aggregated PProDOT configurations and different placements of the transport species. The modeling is conducted under extended equilibration process up to 50 ns and repeated thermal annealing. Extensive structural characteristics, including the X-ray diffraction (XRD) patterns, end-to-end distances of PProDOT chains, and local coordination environments are analyzed to confirm the reproducibility of the modeling results. Details are described in the following Methodology section. This work focuses on the fundamental understanding of the molecular motifs underpinning the breathing strain of conducting polymers and provides a theoretical guidance on the selection of the electrolyte in regulating the mechanical response of OMIECs.

Methodology

Force field parameters and modeling programs: The general Amber force field (GAFF)[36] is employed to describe the bonding and non-bonding interactions in PProDOT. The effectiveness of GAFF to reproduce the morphological features of conjugated polymers, including the π-π stacking and lamellar stacking, has been demonstrated by previous literature.[31,37,38] Gaussian16[39] is employed for the geometric optimization, calculating the vibrational frequency of

ProDOT, and determining electrostatic potential (ESP) derived partial charges[40] of PProDOT at oxidized states using wb97xd/6-31G(d) functional and basis set. Spin multiplicity of the ground state of PProDOT at each oxidation level is determined following a prior density functional theory (DFT) study on poly(3,4-ethylenedioxythiophene) (PEDOT) with the same functional and basis set. [41]

GAFF-compatible force field parameters are taken for Li^+, BF_4^-, ClO_4^-, PF_6^-, $TFSI^-$, PC, EC, and DEC. [42–45] The initial configurations for both self-aggregated PProDOT and its swelling behavior within the electrolyte are built in Packmol.[46] MD simulations are conducted using Large-scale Atomic/Molecular Massively Parallel Simulator (LAMMPS).[47] Antechamber[48] and fftool[49] are utilized to compile the topology-related input files for LAMMPS. Three-dimensional (3D) periodic boundary conditions (PBCs) are applied for all the MD simulations. Long-range electrostatic interactions are computed using the particle-particle particle-mesh (PPPM) method[50] and the cutoff distance is set as 12 Å. The dielectric constant for PProDOT and the damping parameter for Langevin dynamics are selected according to the previous literature.[11] Various analyses including XRD patterns, radial distribution function (RDF) profiles, cumulative coordination numbers (CNs), and mean square displacements (MSDs) are calculated in LAMMPS. Other data post processing is performed in customized MATLAB codes and visualization is conducted using OVITO.[51]

Self-aggregated PProDOT: A PProDOT chain is composed of 12 ProDOT monomers, a length deemed sufficient for simulating the mechanical response. This choice is further elaborated in the Results and Discussion. Larger polymer chain models consisting of more monomers would make the computation prohibitively expensive. Initially, 50 charge neutral PProDOT chains are randomly positioned without overlap in a simulation box of the size of 120×120×120 $Å^3$, followed

by energy minimization via the conjugate gradient (CG) algorithm. We prepare three different initial configurations, namely configuration 1, 2, and 3. Subsequently, all the three configurations are relaxed under the isothermal–isobaric (NPT) ensemble at 303 K and 1.0 atm for 5 ns. To help overcome energy barriers of structural relaxation and escape from local minima, thermal annealing is applied. More specifically, the temperature increases from 303 K to 503 K over 3 ns, is held at 503 K for 10 ns, and then decreases from 503 K to 303 K in 5 ns. Despite the lack of direct experimental measurement of the glass transition temperature (T_g) of PProDOT, T_g of PEDOT:PSS was reported between 333 K and 343 K and its decomposition temperature is 573 K.[52] A thermal annealing temperature of 503 K is widely used in MD simulations of other conjugated polymers, such as p(g2T-TT) and p(g2T2).[11,12] Here we adopt the same annealing temperature of 503 K. Configuration 1 is finally held for equilibration at 303 K and 1.0 atm under NPT ensemble for 10 ns. The same equilibration at 303 K and 1.0 atm under NPT ensemble but up to 50 ns is conducted for configuration 2. In configuration 3, a repeated thermal annealing using the same temperature profile is applied, and then followed by equilibration at 303 K and 1.0 atm under NPT ensemble for 50 ns. Throughout the thermal annealing and equilibration, the implicit solvent effect is considered via Langevin dynamics to speed up the conformational sampling of PProDOT.[53] The converged structural characteristics, including the XRD patterns, coordination numbers, and the end-to-end distances, show that the three configurations reach the equilibrium state following the thermal annealing and equilibration processes as shown in Figure S1. The average mass density of the self-aggregated PProDOT is 1.017 g/cm^3.

Mechanical swelling upon doping: The generated self-aggregated PProDOT (configuration 1) is immersed in different electrolytes to compare its swelling behavior. For ease of reference, Table S1 summarizes the modeling system consisting of 0.2 M and 1.0 M $LiClO_4$ in PC, 1.0 M $LiBF_4$,

$LiPF_6$, and LiTFSI in PC, and 1.0 M $LiPF_6$ in EC/DEC with 1:1 volume ratio. The mixing is accomplished by surrounding PProDOT by 15000 organic solvent molecules, 1275 Li^+ and 1275 anions for 1.0 M electrolytes, and 275 Li^+ and 275 anions for 0.2 M electrolyte within a larger simulation box of the size of 140×140×140 $Å^3$. Energy minimization is performed via the CG algorithm, followed by equilibration under NPT ensemble at 303 K and 1.0 atm for 10 ns. To mimic the doping process of PProDOT, charges corresponding to the specific oxidation state are updated for PProDOT, while an equivalent number of anions are randomly placed in the surrounding electrolyte. For PProDOT, 1 additional hole on each 12-monomer chain corresponds to the oxidation level of 8%, likewise, 2, 3, and 4 additional holes correspond to the oxidation levels of 16%, 25%, and 33%, respectively. Finally, the system is equilibrated under NPT ensemble at 303 K and 1.0 atm for 10 ns. Both experimental studies and first-principle calculations have demonstrated that the oxidation level of pristine PEDOT reaches 33% upon doping,[54–56] which has been adopted for other conjugated polymers such as poly-[3,3'-bis(2-(2-(2-methoxyethoxy)ethoxy)ethoxy)-2,2'-bithiophene] (p(gT2)).[11,12] In the modeling, we assume the upper limit of 33% for PProDOT oxidation. To validate the equilibration protocol and reproducibility of the simulation results, we repeat the modeling using self-aggregated PProDOT models of distinct initial configurations and an extended equilibration time. Specifically, configuration 2 is immersed in 0.2 M and 1.0 M $LiClO_4$ in PC, with different placements of initial positions of salt and organic solvents compared to those in configuration 1. Afterwards, the models are equilibrated under NPT ensemble at 303 K and 1.0 atm up to 20 ns. The comparison is included in the Supporting Information and will be discussed later.

Results and Discussion

The upper panel in Figure 1a shows the chemical structure of ProDOT. The lower panel shows the optimized unit through DFT modeling and highlights the non-planarity of ProDOT, with the branched side chain (the R groups in the chemical structure) extending out of the π-conjugated plane – a feature ascribed to the propylene bridge.[57] Based on the ProDOT, the PProDOT chain is built consisting of 12 monomers. The rationalization of the choice of 12 monomers per chain is as follows. First, a previous study obtained comparable computed XRD patterns of PEDOT with the chain lengths of 3, 6, 12, and 18 monomer units, which agree well with the experimental data. Thus, the authors concluded that the morphology of PEDOT is not dependent on the chain length.[37] Second, since our modeling examines multiple oxidized states of PProDOT, a precise description of the corresponding electronic structures is crucial. A prior DFT calculation showed that a 12-monomer chain enables a sufficient description of the electronic structure of PEDOT at oxidation levels ranging from 0% to 50%.[41] Additionally, the bulky branched alkyl side chain on PProDOT is for better solubility without a significant influence on its electronic structure.[3,32] Therefore, it is reasonable to assume that a 12-monomer PProDOT chain adequately describes the electronic structures over the oxidation levels examined in this study. Figure 1b displays the self-aggregated PProDOT (configuration 1). The structure is unwrapped over the PBCs using OVITO according to the periodic image information output in the trajectory file. Grazing-incidence small-angle X-ray scattering (GIWAXS) showed that PProDOT is structurally isotropic.[57] Therefore, we generate the self-aggregated PProDOT with randomly placed polymer chains. Figure 1c displays the self-aggregated PProDOT soaked in the electrolyte environment.

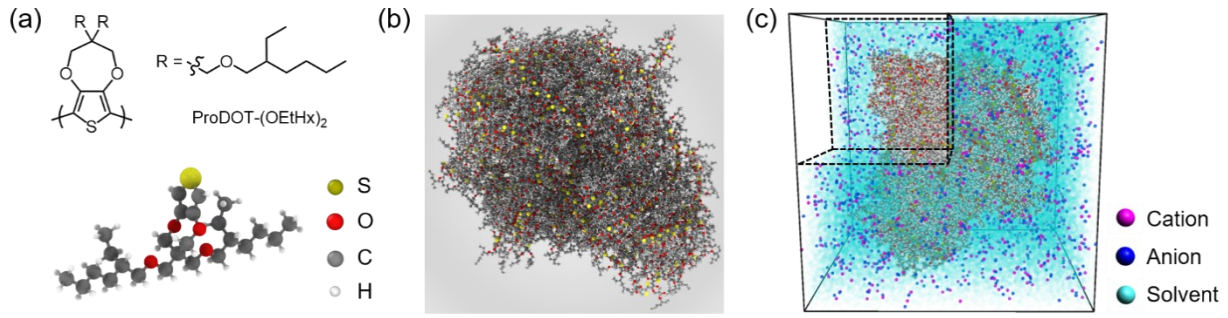

Figure 1. Material and model. (a) Upper panel: the chemical structure of ProDOT-$(OEtHx)_2$; Lower panel: the unit of ProDOT-$(OEtHx)_2$ after structural optimization. ProDOT is non-planar, and the side chains (R groups) extend out of the π-conjugated plane due to the propylene bridge. (b) The self-aggregated PProDOT model consists of 50 chains and each chain contains 12 monomers. (c) The self-aggregated PProDOT soaked in the electrolyte containing cations (magenta), anions (blue), and solvents (cyan). 1/8 of the simulation box at the upper left corner is hidden for better illustration of the relative positions between PProDOT and the electrolyte.

The structural characterization of PProDOT is elaborated as follows. We note that, owing to the nearly identical structural characteristics of self-aggregated PProDOT generated from different initial configurations (Figure S1), the following discussion is based on equilibrated configuration 1 of the PProDOT model. The left panel of Figure 2 presents the calculated XRD pattern of PProDOT (black line) where the broad peaks indicate an amorphous nature of the morphology. Furthermore, the XRD patterns of the thiophene groups (red line) and the remaining atoms (blue line) in PProDOT are separately computed where the peak centers are identified. Following $d = \frac{\lambda}{2\sin\theta}$,[58] the distance d associated with the diffraction angle 2θ is calculated. λ is the wavelength of the incident beam, which is 1.541 Å for Cu Kα radiation.[59] The peak (I) in the XRD pattern of the thiophene groups centers around 24^{o}, corresponding to the distance d of 3.7 Å. As seen from the representative snapshot of the molecular structure (left top in the right panel of Figure 2), this diffraction peak is attributed to the distances between the end carbon atoms of dihedral angles in the thiophene groups. This observation is part of the features of a 'straight' chain configuration, which can be understood by the persistence length. Earlier studies showed that the persistence length of a 12-monomer PEDOT chain extends to nearly 12 monomer units around

300 K.[60] It is also interesting to note that the diffraction peaks such as (I) are often associated with the π − π stacking in other π -conjugated polymers including PEDOT and glycolated polythiophenes.[12,29,38,61,62] However, π − π stacking is barely observed in PProDOT. This result agrees with the GIWAXS measurement.[57,63] As shown in Figure 1a, the protrusion of the branched side chains from the π-conjugated plane prevents PProDOT forming π − π stacking, instead it results in an open and less dense structure. Moreover, the lamellar stacking in the GIWAXS measurement[57] is not observed in the calculated XRD pattern. A prior study stressed the importance of the substrates in the formation of lamellar stacking in PEDOT.[64] Since the GIWAXS experiment was conducted for PProDOT bonded to a substrate, while the generated PProDOT in this work is a free-standing film, this difference might explains the absence of lamellar stacking in the self-aggregated PProDOT.

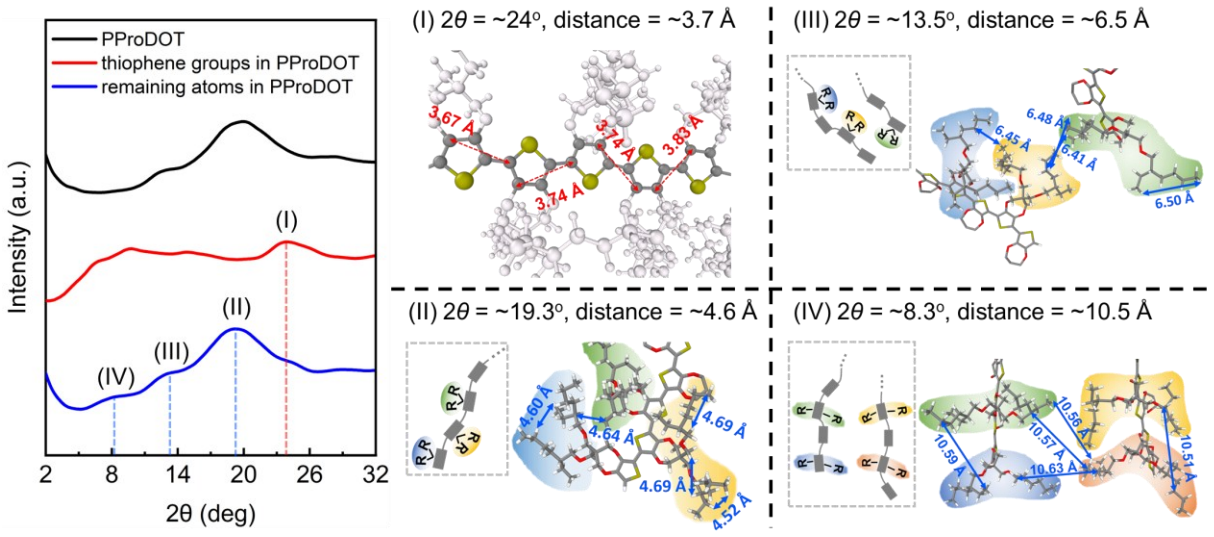

Figure 2. Structural characterization of the self-aggregated PProDOT. Left panel: calculated XRD patterns of PProDOT (black), the thiophene groups (red), and the remaining atoms (blue) in PProDOT. The broad diffraction peaks indicate an amorphous morphology. Four broad peaks are labeled as (I), (II), (III), and (IV) and their corresponding atomic distances are illustrated in the right panel. Right panel: snapshots of representative molecular structures with marked atomic distances contributing to the diffraction peaks. The inset figures are schematics where the grey block represents ProDOT and R represents the side chain. The

peak (I) is attributed to the distance between the end carbon atoms of dihedral angles in the thiophene groups. No specific atom pairs are designated to the peaks (II), (III), and (IV). Nevertheless, (II) mainly corresponds to the distance between the intrachain atoms, (III) is related to the distance between both inter- and intra- chain atoms, and (IV) is mainly associated with the distance between interchain atoms.

For the remaining atoms in PProDOT, three broad peaks in the diffraction pattern are labeled as (II), (III) and (IV), which center at $\sim 19.3^{o}$, $\sim 13.5^{o}$, and $\sim 8.3^{o}$, and correspond to the distances of ~ 4.6 Å, ~ 6.5 Å, and ~ 10.5 Å, respectively. The right panel of Figure 2 shows the representative snapshots of the molecular structure where the distances are annotated. Schematic diagrams of the MD snapshots enclosed by grey dashed boxes are also included for better illustration, where ProDOT is represented by the dark grey blocks, and R designates the side group. In addition, the R groups connected to the same ProDOT unit are marked in the same color. Upon screening the distance over all atom pairs besides the thiophene groups in PProDOT, it is found that, unlike the peak (I), no specific atom pairs are designated to the peaks (II)-(IV). The peak (II) is mainly associated with the distance between the intrachain atoms (60%), while (III) correlates to the distance between both the intrachain and interchain atoms (46% and 54%, respectively), and (IV) primarily originates from the distance between the interchain atoms (71%). In the following discussion on mechanical swelling, the position and intensity changes in these four peaks will help identify the morphological evolution of PProDOT upon doping.

After validating the structure characteristics, the self-aggregated PProDOT is immersed into the electrolyte to examine its structural response and mechanical swelling (Figure 1c). Prior experiments showed little electrochemical conditioning in PProDOT in the cyclic redox reactions owing to its open molecular structure.[20,21] Therefore, the swelling behavior of the dry pristine PProDOT in the liquid electrolyte during the initial oxidation is representative to its breathing activation over cycles. For the conjugated polymers of strong electrochemical conditioning, it is necessary to invoke multiple cycles to reach a stable structural response.

Mechanical swelling upon doping: We calculate the swelling volume, defined as the change of molecular volume divided by the initial volume at the dry pristine state, of PProDOT at various oxidation states (i.e., 0%, 8%, 16%, 25%, and 33%), and examine the underlying microstructural mechanism. In addition, we analyze the evolution of the solvation structure and the transport property of the electrolytes to provide insight on the kinetics. Figure 3a-e show the final equilibrated states of PProDOT in 1.0 M $LiClO_4$ in PC at each oxidation level, demonstrating the gradual volumetric expansion upon oxidation. For better visualization, Li^+ and ClO_4^- are not shown in the MD snapshots. Given the irregular shape of the PProDOT model, determining the exact volume of the molecular structure enclosing all the edges and corners is difficult. This makes a quantitative measure of the post-absorption swelling of PProDOT challenging. Here we introduce a reference box within the polymer network, whose size is determined by the number density profile, for ease of calculating the swelling volume. As described earlier, the self-aggregated PProDOT is first unwrapped across the periodic boundaries, and then placed in a larger box of the size of $140\times140\times140$ $Å^3$, where the center of mass of PProDOT coincides with the center of the box. The density profiles of PProDOT along the *x*, *y*, and *z* directions are plotted as shown between Figure 3a and b with the coordinate defined in Figure 3a. Along each direction the number density reaches a plateau from -20 Å to 20 Å, as marked by the maroon dashed box, highlighting the densest segment of the PProDOT model. The dense segment is then used to determine the boundaries of the reference box shown in Figure 3a. Subsequently, after the swelling of PProDOT reaches equilibrium at a given oxidation level, the volume of the electrolyte absorbed into the reference box is calculated using the Zeo++ code.[65] The ratio between the volume of the absorbed electrolyte and the volume of the initial reference box (remaining constant at all oxidation states) represents the swelling volume which is plotted in Figure 3f. The inset MD snapshots only

show the absorbed species of ClO_4^- anions, Li^+ cations, and PC solvent in the reference box and PProDOT is hidden for better visualization.

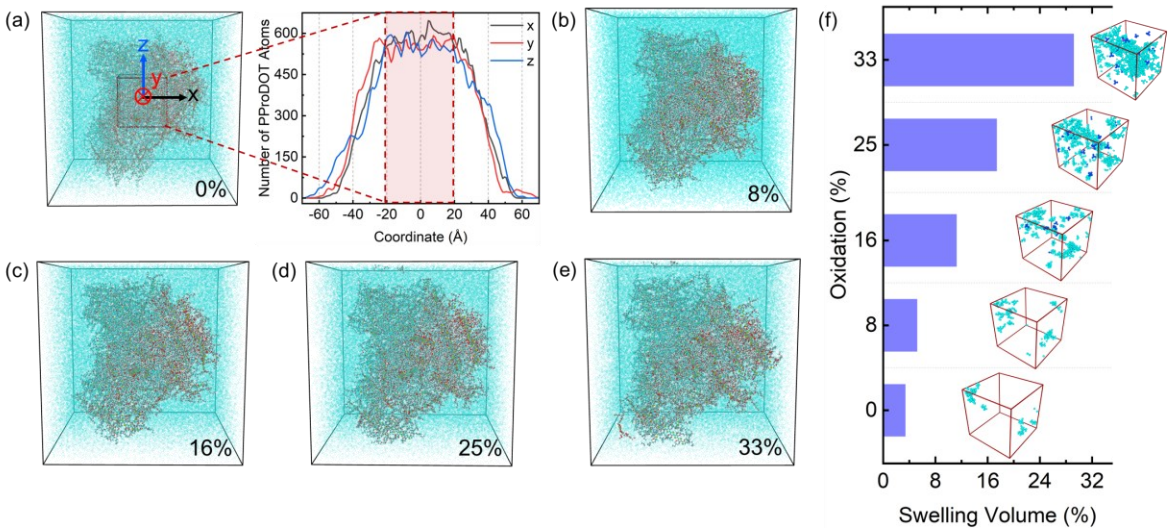

Figure 3. PProDOT swelling in the electrolyte composed of 1.0 M $LiClO_4$ in the PC solvent at different oxidation levels. (a-e) Snapshots of PProDOT at the equilibrium state of the oxidation level of 0%, 8%, 16%, 25%, and 33%, respectively, demonstrating a gradual increase of volume upon oxidation. The ions (Li^+ and ClO_4^-) are not shown for better illustration. (f) Swelling volume of PProDOT relative to the pristine dry state. Inset are the snapshots of the reference box, as illustrated in (a), for the volume calculation. The box is selected based on the number density profile of the self-aggregated PProDOT along the *x*, *y*, and *z* directions. In these inset snapshots, only the absorbed species including ClO_4^- (blue), Li^+ (magenta), and PC (cyan) are shown to demonstrate mass transport of the electrolyte into PProDOT.

During the electrolyte absorption, PProDOT chains rearrange to accommodate the injected electrolyte. To understand the mechanical swelling, we analyze the microstructural evolution of PProDOT and inter/intrachain changes. The left panel in Figure 4a presents the normalized average end-to-end distance of PProDOT chains at each oxidation level. The end-to-end distance is calculated by the distance between the two end hydrogen atoms on the two terminal thiophene groups in a PProDOT chain as shown in the inset of Figure 4a. The average end-to-end distance of self-aggregated PProDOT chains is used as the reference for normalization. The error bars are calculated by dividing the standard deviation by the average end-to-end distance of the 50 PProDOT chains. The average end-to-end distance of self-aggregated PProDOT chains is 44.5 Å,

close to the contour length of 47.23 Å, which denotes the relatively straight chain configuration. This feature is described with the XRD pattern in Figure 2 and is understood by the persistence length as discussed earlier. In the charge neutral state (0%), the passive swelling of the dry PProDOT in the liquid electrolyte is limited and PProDOT chains extend very little. As PProDOT are oxidized, despite the active absorption of the charged species and the organic solvent, extension of the chain length remains negligible. This is due to the straight and rigid chain configuration as well as the fact that the absorbed electrolyte primarily resides in the flexible sidechain domain, which will be discussed in detail in Figure 4b. To facilitate visualization of the microstructure, the PProDOT chains are extracted and demonstrated in the right panel of Figure 4a by hiding the surrounding electrolyte in the model and unwrapping atoms across the periodic boundaries in the charge neutral (0%) and oxidized (33%) states. Besides, the remaining atoms except the thiophene groups in PProDOT are greyed out. Hence, the chain configurations can be seen and compared in the two oxidation states.

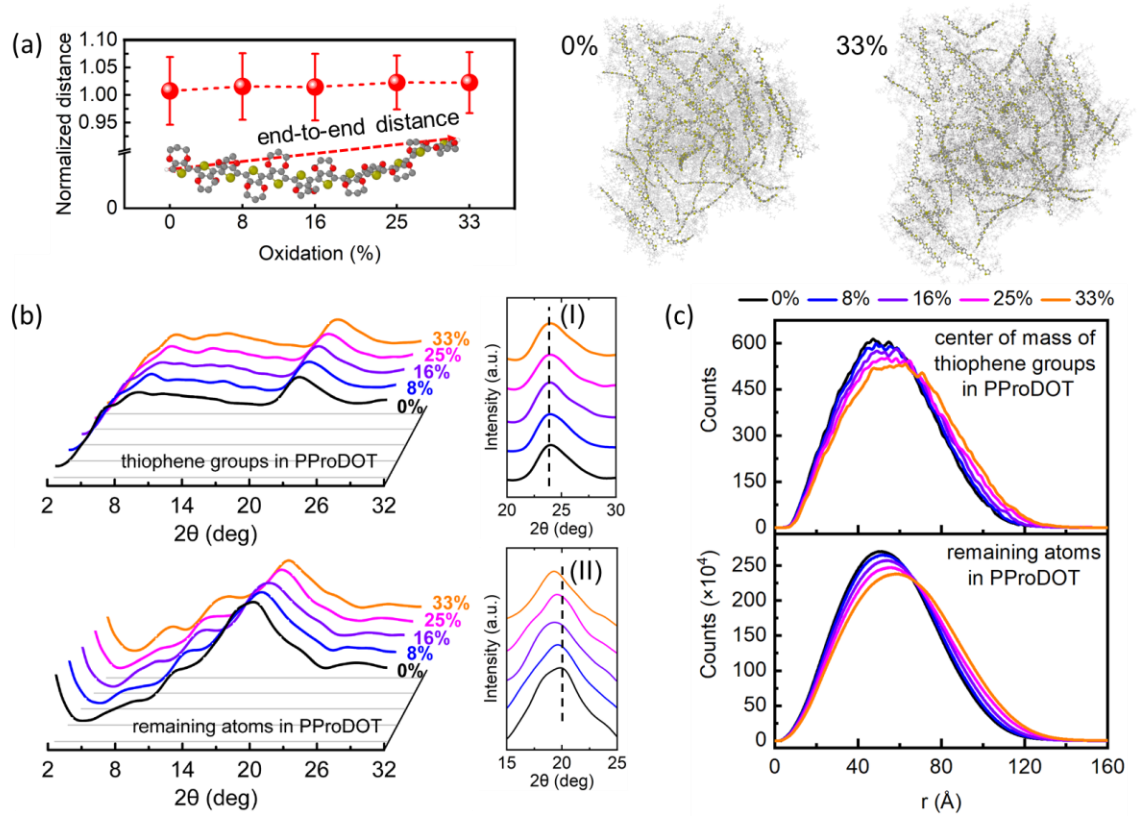

Figure 4. Structural characterization of PProDOT upon oxidation from 0% to 33% with 1.0 M $LiClO_4$ in PC. (a) Left panel: normalized average end-to-end distance of PProDOT chains. The inset figure demonstrates the end-to-end distance which is calculated between the two end hydrogen atoms in the two terminal thiophene groups of a PProDOT chain. The side chains are not shown for better illustration. The average end-to-end distance of self-aggregated PProDOT chains in the pristine dry state is used as the reference value for normalization. Error bars are calculated from the standard deviation of the 50 chains divided by the average value. Right panel: MD snapshots of PProDOT at the oxidation level of 0% and 33%. The molecular chains mostly retain their rigid configuration upon oxidation. (b) Left panel: Calculated XRD patterns of the thiophene groups and the remaining atoms in PProDOT. The structural features associated with the diffraction peaks are discussed in Figure 2. Right panel: Zoomed-in view of XRD patterns. (c) Differential coordination numbers of the centers of mass (COMs) of the thiophene groups and the remaining atoms in PProDOT.

Figure 4b shows the calculated XRD patterns of the thiophene groups and the remaining atoms in PProDOT. At different oxidation states of PProDOT, the XRD patterns of the thiophene groups are nearly identical, indicating little change of the distances between the end carbon atoms of dihedral angles. This is also consistent with the end-to-end distance of PProDOT chains shown in Figure 4a. In contrast, the XRD patterns of the remaining atoms show apparent changes. More specifically, the peaks around 8.3° and 13.5° become progressively more intense upon oxidation.

This suggests more atom pairs of large intrachain and interchain distances. Meanwhile, the peak around 19.3° shifts towards a smaller diffraction angle 2θ and the peak intensity diminishes, which implies larger intrachain distance and less atom pairs with small intrachain distances. The shifts in diffraction peaks are attributed to the swelling of PProDOT. The observations also corroborate with the absorption of the electrolyte predominantly in the flexible sidechain domain. Further evidence of the morphological evolution is provided by the differential CNs of the centers of mass (COMs) of the thiophene groups and the remaining atoms in PProDOT (Figure 4c). The COMs of the thiophene groups or remaining atoms from the same chain have been excluded in the calculation. Therefore, Figure 4c only represents the interchain information without counting for the intrachain changes. The peak shift of the CNs towards a larger radial distance and the reduced peak intensity of the CNs both indicate the increased interchain distances among the PProDOT network to accommodate the oxidation and absorption of the electrolyte.

After determining the swelling volume and examining the morphological characterizations, we aim to study the swelling mechanism. Several intertwined factors contribute to the volume change of PProDOT upon oxidation, including (I) volume expansion caused by electrostatic repulsion among the positively charged PProDOT chains, (II) volume shrinkage induced by electrostatic attraction between PProDOT and the compensating anions and also the screened electrostatic repulsion among PProDOT chains due to the anions, (III) volume expansion due to the mass transport of anions into PProDOT without counting for the electrostatic interactions, and (IV) volume expansion induced by the absorption of the organic solvent. Since the long-range Coulombic interactions are computed with the PPPM method and 3D PBCs, charge neutrality of the system must be preserved all the time, making the examination of the factor (I) in solely oxidized PProDOT unfeasible. Compensating anions, apart from those in the electrolyte, are

necessary to balance the positive charges in PProDOT during oxidation. Here we prepare two model systems against the self-aggregated PProDOT to differentiate the contributions of electrostatic interactions and mass transport to the mechanical swelling. The first model system includes oxidized PProDOT (33%) and 200 surrounding BF_4^- anions, and the second one contains oxidized PProDOT (33%) with 1.0 M $LiBF_4$ in PC and additional 200 surrounding BF_4^- anions. BF_4^- is chosen for its smallest ionic radius among the anions we study in this work. Overall, the system of oxidized PProDOT (33%) with BF_4^- considers the contributions of factors (I)-(III) to the volume change of PProDOT, while the system of oxidized PProDOT (33%) with 1.0 M $LiBF_4$ in PC and extra BF_4^- considers all the four contributing factors especially the mass transport of the solvent. After equilibration of the systems for 10 ns, the cumulative CNs between the PProDOT atoms are calculated and shown in Figure 5a. Compared to the self-aggregated PProDOT, the volume of oxidized PProDOT (33%) increases by 5.1 % in the presence of BF_4^- anions, and the CNs profiles are nearly overlapping. However, when the mass transport of the solvent is enabled, volume expansion reaches 21.3%, accompanied by a considerable reduction of the CNs. Therefore, the key mechanism that drives the mechanical swelling of PProDOT is the absorption of the electrolyte, especially the mass exchange of the organic solvent, compared to the local electrostatic interactions of the charged species. This indicates that mechanical activation of the conducting polymers in solid-state devices, such as solid-state OECDs in commercial use, can be largely suppressed where the flow of the organic solvent is prohibited.

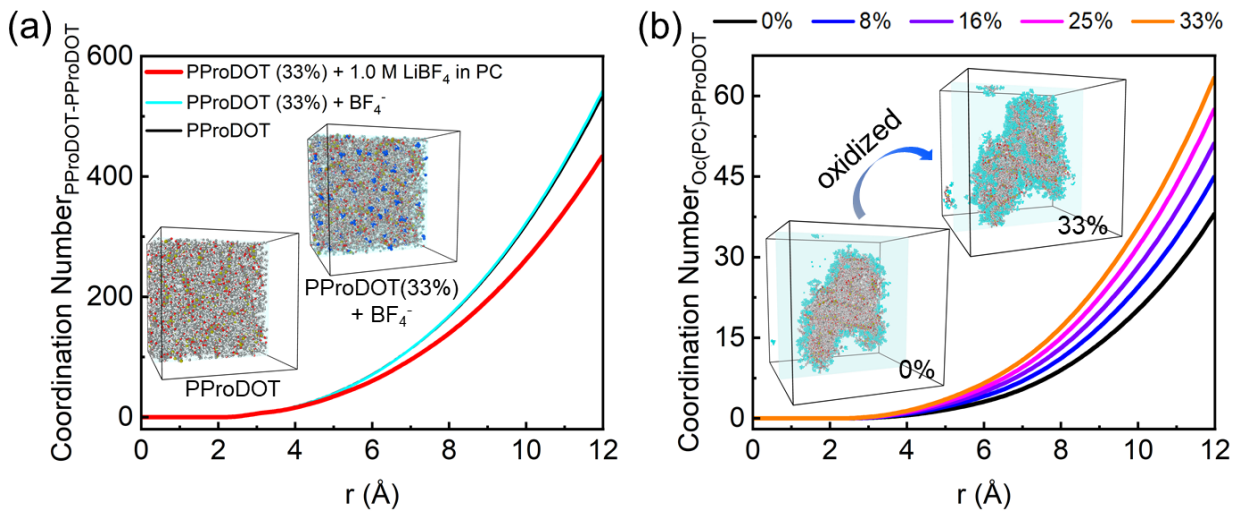

Figure 5. Comparative studies of the swelling mechanism. (a) Cumulative CNs between the PProDOT atoms in self-aggregated pristine PProDOT, oxidized PProDOT (33%) with 200 charge-compensating BF_4^- anions, and oxidized PProDOT (33%) in the electrolyte of 1.0 M $LiBF_4$ in PC with additional 200 BF_4^- anions. Inset shows MD snapshots of self-aggregated PProDOT and its oxidized state with BF_4^-. (b) Cumulative CNs between carbonyl O (Oc) in PC and PProDOT. Inset figures show the charge neutral (0%) and oxidized (33%) PProDOT and neighboring PC molecules (within 3.0 Å to PProDOT).

To further demonstrate the electrolyte absorption into the polymer network, we calculate the cumulative CNs between the carbonyl oxygen (Oc) atoms in PC and PProDOT (Figure 5b), as well as those between O in ClO_4^- and PProDOT (Figure S2). The increase in the CNs is the direct evidence of electrolyte penetration as PProDOT is oxidized. The visualization is provided by the inset figures, which show the MD snapshots of the charge neutral (0%) and oxidized (33%) PProDOT and the PC molecules (cyan color) within 3.0 Å to PProDOT. Similarly, the inset figures in Figure S2 show the MD snapshots of the charge neutral (0%) and oxidized (33%) PProDOT and ClO_4^- within 3.5 Å to PProDOT. All other electrolyte species have been hidden, and the cross sections of the sliced simulation boxes are used to demonstrate the penetration of PC and ClO_4^- into PProDOT. We note that the cutoff distances of 3.0 Å and 3.5 Å are arbitrarily chosen for the illustration purpose. They do not represent any physical bonding distances in the system and are simply used to demonstrate the neighboring environment of PProDOT with the organic solvent and anions.

We explore the transport property of the cation, anion, and organic solvent in the mixture of PProDOT with the electrolyte as well as the evolution of the solvation structure within the electrolyte to understand the kinetics behind the mechanical swelling. Starting from the energetically optimized configuration, the system is allowed to dynamically equilibrate at 303 K for 10 ns, which induces substantial mixing of the constituent species. The random walking is far beyond the local elementary hopping. We calculate the mean square displacements (MSDs) by the definition MSD=$\langle|r_i(t) - r_i(0)|^2\rangle$, where $r_i(t)$ is the position of the species *i* at the time *t*, $r_i(0)$ is the position in the initial configuration, and $\langle\ \rangle$ represents an average over the ensemble. Figure 6a shows the MSDs of Li^+, ClO_4^-, and the solvent PC against time when PProDOT is at the oxidized state (33%). A linear relationship is observed after the initial equilibration period for all the three species, which indicates diffusion dominated kinetics. The MSDs between 4 ns and 10 ns are used for linear fitting, which are shown in grey lines with their analytical expressions as well as the coefficients of determination (R^2). Subsequently, diffusion coefficients are calculated using the Einstein relation $D = \lim_{t\to\infty} \frac{1}{6t} \left\langle \left| r_i(t) - r_i(0) \right|^2 \right\rangle$.[66] Figure 6b summarizes the diffusion coefficients of the cation, anion, and solvent when PProDOT is at each oxidation state. In the charge neutral state of PProDOT, the diffusion coefficients agree well with those reported in the electrolytes.[67] The diffusion coefficient of Li^+ is the smallest due to the bulk and stable solvation shell, followed by ClO_4^- and PC. As PProDOT is oxidized, the diffusion coefficients of ClO_4^- and PC slightly decrease with a minor fluctuation at the oxidation level of 8%. This decreasing trend is attributed to the electrostatic attraction between the negatively charged ClO_4^- and Oc in PC and the positively charged PProDOT. Even though the positive charges are primarily located on the backbone of PProDOT upon oxidation,[7,11,68–70] ClO_4^- and PC preferentially accumulate in the flexible side chain regions as discussed earlier. Given the relatively open structure of PProDOT,

the influence of electrostatic attractions on the diffusion coefficients of ClO_4^- and PC is not significant. More interestingly, the diffusion coefficients of Li^+ and ClO_4^- appear to converge at the end of oxidation. This is an outcome of the mass transport of PC into PProDOT, which in turn leads to the solvent consumption in the solvation shell of Li^+ and formation of the contact ion pairs between Li^+ and ClO_4^-. This feature can be validated by analysis on the solvation structure in the electrolyte. Figure 6c shows the RDF and cumulative CNs between Li^+ and Oc in PC. The inset provides an enlarged view of the CNs highlighted in light cyan. At the charge neutral state of PProDOT, the first peak in RDF is located at 2.675 Å, larger than the reported value of ~2 Å in the pure electrolyte.[71,72] Besides, the first solvation shell around Li^+ extended to 4 Å with the CN being 3.5 that is below the literature value of 4~6.[73–75] These discrepancies are mainly due to the presence of PProDOT in the model. Unlike pure electrolyte, PProDOT disrupts the continuity of the solvation structure. For instance, the charge neutral PProDOT is surrounded by PC (as shown in the inset of Figure 5b) which reduces the availability of PC to dissociate Li^+. In addition, the dielectric constant makes a difference. In LAMMPS, one dielectric constant is set for the multi-component system, and its value is taken as 5 primarily due to the PProDOT. This value is well below 64.92 which is the dielectric constant for PC at 25 °C.[76,77] Therefore, the ability of PC to dissociate Li^+ is reduced in the simulation, resulting in the larger separation between Li^+ and Oc in PC, less PC in the first solvation shell of Li^+, and more contact ion pairs. A prior study reported a decrease in the CN between Li^+ and the solvent from 4 in PC to 3.3 in DEC with the dielectric constant of 2.8 at 25 °C.[78] Upon oxidation of PProDOT, the position of the first peak in RDF remains unchanged but the peak density reduces. Meanwhile, the CN decreases from 3.5 to 2.9 due to the absorption of PC into PProDOT at the expense of the reduced coordination with Li^+.

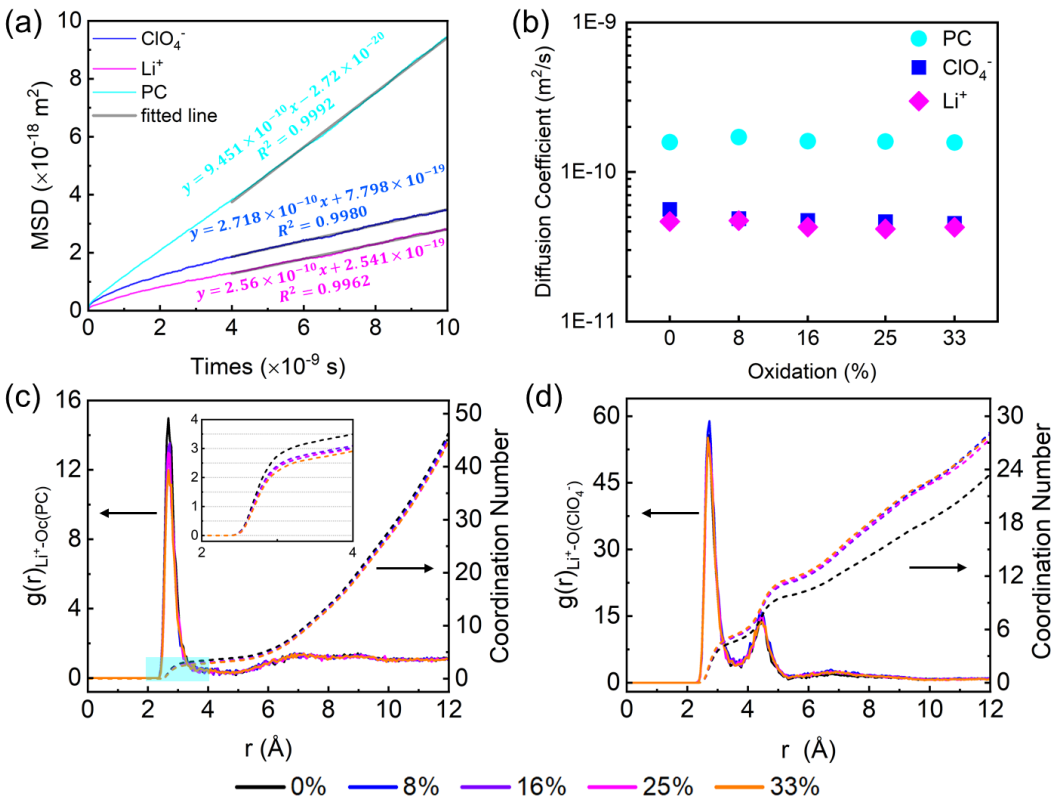

Figure 6. Transport kinetics. (a) MSDs of ClO_4^-, Li^+, and PC with respect to time when PProDOT is at the oxidized state (33%). MSDs between 4 ns to 10 ns are used for linear fitting. (b) Diffusion coefficients of ClO_4^-, Li^+, and PC calculated from the MSDs. (c) RDF and cumulative CNs between Li^+ and Oc in PC. Inset is the enlarged figure of the CNs shaded in light cyan. (d) RDF and cumulative CNs between Li^+ and O in ClO_4^-.

To validate the increased number of contact ion pairs in the mixture of PProDOT and electrolyte, the RDF and cumulative CNs between Li^+ and O in ClO_4^- are illustrated in Figure 6d. In the pure electrolyte of 1.0 M $LiPF_6$ in EC, two peaks were observed in the RDF between Li^+ and P in PF_6^- with a large intensity of the second peak, suggesting a prevalence of solvent separated ion pairs compared to the contact ion pairs.[79] In comparison, at the charge neutral state of PProDOT, the first peak in RDF is more pronounced, indicating an abundance of contact ion pairs. This is ascribed to the presence of PProDOT and/or the dielectric constant as discussed above. When PProDOT is oxidized, the peak intensity in RDF increases and so do CNs, demonstrating the formation of more contact ion pairs. This is again due to the reduced coordination of Li^+ with

PC, driven by the mass transport of PC into PProDOT, providing more Li^+ to the contact ion pairs with ClO_4^-.

Dependence on the salt concentration in the electrolyte: Thus far, we have presented the studies of mechanical swelling of PProDOT, its microstructural characteristics at different oxidation states, the swelling mechanism, and transport kinetics behind the mechanical response of PProDOT in a representative electrolyte. In the following we will take the same approach to systematically study a variety of electrolytes and explore the underlying molecular mechanism. We first examine the effects of the salt concentration, wherein PProDOT is immersed in 0.2 M and 1.0 M $LiClO_4$ in PC. Figure S3 shows the final equilibrated states of PProDOT at the oxidation level of 33% in the two electrolytes. Apparently, PProDOT soaked in the electrolyte of 0.2 M salt concentration exhibits a larger mechanical swelling compared to the case of 1.0 M counterpart. The swelling volumes of PProDOT are shown in Figure 7a using the same methodology described in Figure 3. The comparison of the modeling result with the prior experimental result of in-situ nanoindentation is also included. The inset MD snapshots show more electrolyte penetration into the PProDOT network with the 0.2 M salt concentration. We note that in in-situ nanoindentation measurements, the swelling volume is influenced by factors apart from the salt concentration, such as the film thickness and the voltage profile including the hold time at the peak voltage and the potential scan rate.[21] These factors are not considered in the simulation which may contribute to the discrepancy in their comparison.

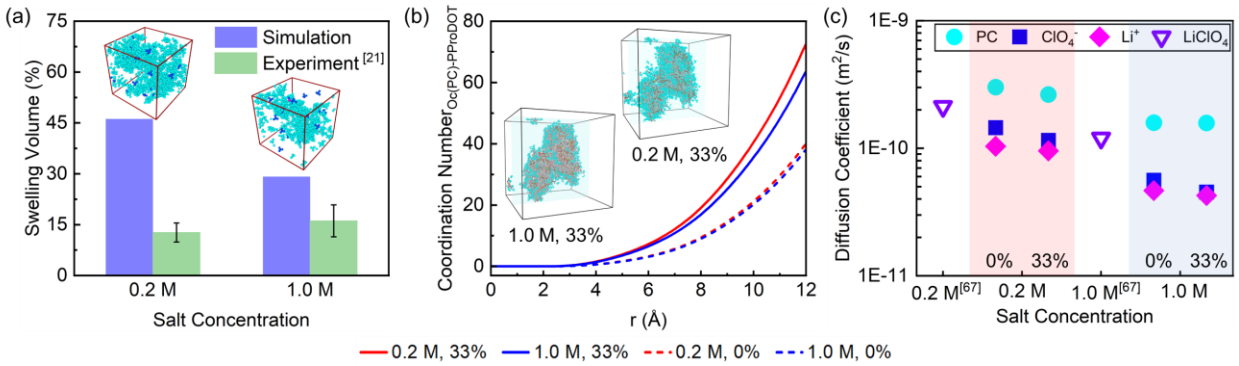

Figure 7. Effects of salt concentration. (a) Comparison of the swelling volumes of PProDOT with $LiClO_4$ in PC at two different salt concentrations. The inset snapshots only show the absorbed electrolyte including ClO_4^- (blue), Li^+ (magenta), and PC (cyan) in the reference box of PProDOT where the swelling volume is determined. (b) Comparison of the cumulative CNs between Oc in PC and PProDOT upon oxidation with two different salt concentrations. Inset figures show the cross-section view of oxidized PProDOT and neighboring PC (within 3.0 Å to PProDOT). (c) Diffusion coefficients of PC, ClO_4^-, and Li^+ with two different salt concentrations when PProDOT is at the charge neutral (0%) and oxidized (33%) states. Binary (molecular) diffusion coefficients of $LiClO_4$ in PC at 298 K measured by the Moiré pattern method[67] are plotted for comparison, which shows good agreement.

The structural characteristics are demonstrated by the calculated XRD patterns and differential CN profiles (Figure S4). The XRD patterns of the thiophene groups (upper panel of Figure S4a) are nearly identical in the electrolytes of the two different salt concentrations at the same oxidation states (0% and 33%). For the remaining atoms, upon oxidation of PProDOT, the diffraction peak around 19.3° diminishes, while the peaks around 8.3° and 13.5° intensify in both electrolytes. This behavior is consistent with the earlier discussion about the oxidation induced morphological change of the chain structure. More interestingly, at the charge neutral state of PProDOT, the XRD patterns of the remaining atoms in both electrolytes are comparable, however, at the oxidized state (33%), the reduction in the peak intensity around 19.3° as well as the increase around 8.3° and 13.5° are more pronounced in the lower-concentration electrolyte. This is a result of the larger volume swelling of PProDOT with 0.2 M salt concentration. Figure S4b shows that, after the passive swelling of PProDOT (0%), both the differential CNs of COMs of the thiophene groups and the remaining atoms in PProDOT are similar in the two electrolytes, however, the CN

profiles in the dilute electrolyte show more significant shift toward a larger radial distance upon oxidation of PProDOT which accommodates the mechanical swelling.

As we have pinpointed the swelling mechanism of the conducting polymer primarily due to the absorption of the organic solvent at the doped states, we calculate the cumulative CNs between Oc in PC and PProDOT, Figure 7b, to demonstrate the mass transport of electrolyte into the polymer. The CNs profiles are comparable after the passive swelling of PProDOT (0%) in the two electrolytes. The counts at a given radial distance significantly increase as PProDOT is oxidized, while the change is more pronounced in the dilute electrolyte environment showing more mass absorption of PC into PProDOT. The inset MD snapshots in Figure 7b provide additional visualization of the neighboring environment between PProDOT and the organic solvent, where the PProDOT at the oxidation level of 33% and PC within 3.0 Å to PProDOT are shown. Similar characteristics are evident in the cumulative CNs between O in ClO_4^- and PProDOT (Figure S5), demonstrating more penetration of ClO_4^- into PProDOT in the dilute electrolyte environment.

The effects of the salt concentration on mechanical activation of PProDOT upon oxidation can be understood from the analysis of the solvation structure in the electrolyte. Figure S6a presents the RDF and cumulative CNs between Li^+ and Oc in PC. When PProDOT is at the charge neutral state (0%), the peaks in RDF are of the same position in the two electrolytes, yet the one for the dilute concentration is higher than the other one. This pattern shows a higher population of PC around Li^+ in the lower-concentration electrolyte. Meanwhile, the CN of the Li^+ solvation shell in the electrolyte of 0.2 M salt is 5.4, larger than 3.5 for the 1.0 M case. The results in RDF and CNs agree well with the literature report for pure electrolytes, where a bulkier solvation shell around Li^+ was observed in dilute electrolyte.[79,80] Upon oxidation of PProDOT (33%), the intensities of RDF peaks reduce, while the CN decreases to 4.5 and 2.9 in 0.2 M and 1.0 M salt

concentration cases, respectively. The reduction results from the mass conduction of PC into PProDOT. The difference in the mechanical swelling of PProDOT might be related to more free PC molecules in the dilute electrolyte, which is 15000-275×5.4=13515 in the model, compared to the 1.0 M case (15000-1275×3.5=10537.5), contributing to the volume change of the polymer. This is also evident in the reduction of the CNs. The CN of the solvation shell decreases by 0.9 in the lower-concentration electrolyte while it decreases by 0.6 in the 1.0 M case, indicating more mass exchange of the solvent into PProDOT. Figure S6b shows the RDF and cumulative CNs between Li^+ and O in ClO_4^-. Similarly, the CN is smaller in the dilute electrolyte at the charge neutral state due to the bulkier solvation shell of Li^+ surrounded by the PC molecules leaving less coordination with ClO_4^-. The RDF peak intensities show an opposite trend primarily due to the different average bulk densities in the two electrolytes.

The diffusion coefficients of the cation, anion, and organic solvent at two different oxidation states of PProDOT are shown in Figure 7c. At the charge neutral state (0%), the diffusion coefficients of PC, ClO_4^-, and Li^+ follow the same decreasing order in the dilute electrolyte that is consistent with the 1.0 M case as discussed in Figure 6b. Overall, the diffusion coefficients of the three mobile species are larger in the electrolyte of 0.2 M salt concentration than the 1.0 M counterpart. The same observation was reported in pure electrolytes due to the lower viscosity in the dilute electrolyte.[79,81] The effect of oxidation on the transport properties was discussed in Figure 6b where the diffusion coefficients of ClO_4^- and PC slightly decreased, while the diffusion coefficients of Li^+ and ClO_4^- tend to converge.

To validate the modeling protocol and ensure the reproducibility of the simulation results, we use a PProDOT model of distinct initial configuration, place the ions and solvents at different initial positions when the polymer is soaked in the electrolyte, and extend the equilibration time

from 10 ns to 20 ns, to study the effect of salt concentration. The structural characteristic of PProDOT, the swelling volume, the coordination analysis, and the diffusion coefficients in the two electrolytes are presented in Figure S4 and described in the supporting information.

Dependence on the organic solvent: Next, we examine the dependence of the mechanical swelling on the choice of the organic solvent by immersing PProDOT in 1.0 M $LiPF_6$ in PC and EC/DEC. Figure S8 shows the final equilibrated states of PProDOT at the oxidation level of 33% in the two electrolytes. Unlike the dependence on salt concentration, it is difficult to visually see the difference of the volume changes of PProDOT. Following the same calculation method, Figure 8a shows the swelling volumes as well as their comparison with the experimental results. The volume change achieves over 20% in both the electrolyte environments, and PProDOT in PC swells 3.4% more than that with the EC/DEC solvent. This observation is substantiated by the slightly smaller CNs between the PProDOT atoms in the PC electrolyte at the oxidized state (Figure S9a). Overall, the modeling results are in good agreement with the in-situ nanoindentation experiments. The structural features of PProDOT characterized by the XRD patterns and differential CNs (Figure S9b and c) are comparable in the two electrolytes.

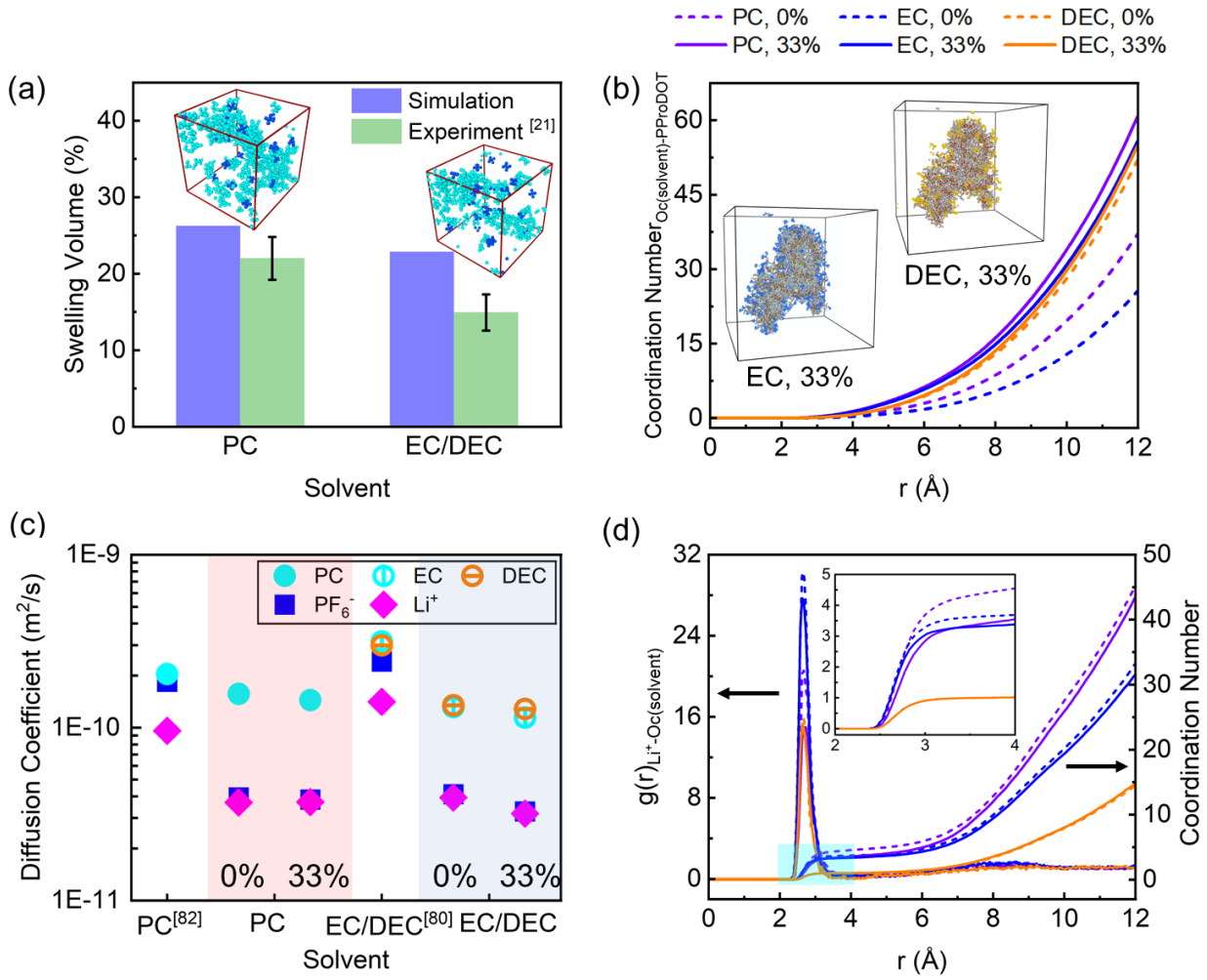

Figure 8. Effects of the organic solvent. (a) Comparison of the swelling volumes of PProDOT with 1.0 M $LiPF_6$ in PC and in 1.0 M EC/DEC. Inset figures show the absorbed electrolyte, including PF_6^- (blue), Li^+ (magenta), and PC (cyan) in the reference box of PProDOT where the swelling volume is determined. (b) Cumulative CNs between Oc in the solvent and PProDOT. Inset shows the MD snapshots of absorbed EC and DEC molecules in PProDOT at the oxidized state (33%). (c) Diffusion coefficients of Li^+, PF_6^-, and the organic solvents. Experimental data from the NMR measurements of 1.0 M $LiPF_6$ in PC[82] and 1.0 M $LiPF_6$ in EC/DEC (1.5:1 mol%) at 303 K[80] are plotted for comparison. EC/DEC = 1:1 vol. % is equivalent to EC/DEC = 1.8:1 mol% (d) RDF and cumulative CNs between Li^+ and Oc in the organic solvents. Inset shows the enlarged CNs shaded in light cyan.

Figure 8b presents the cumulative CNs between Oc in the solvent and PProDOT. After the passive swelling of PProDOT (0%), the CN between Oc in DEC and PProDOT is the largest, followed by Oc in PC and EC with PProDOT. Upon oxidation, the CN between Oc in PC and PProDOT becomes the largest, followed by EC, while the CN between Oc in DEC and PProDOT increases marginally. Such changes of the coordination environments are due to the absorption of

PC and EC into PProDOT, although the slight variation between DEC and PProDOT does not imply little mass transport of DEC into PProDOT or insignificant contribution of DEC to the mechanical swelling of PProDOT. In fact, the inset MD snapshots in Figure 8b, representing the neighboring environment between PProDOT at the oxidized state and EC/DEC which are within 3.0 Å to PProDOT, show otherwise. Clearly, DEC molecules penetrate the PProDOT network just like EC does. More discussions will be given after the analysis of the solvation structure in Figure 8d. The difference between the mechanical swelling of PProDOT in the two electrolytes might be understood in terms of the molar volume of the solvents, which is the ratio of the molar mass to the density. The molar volume of PC (140.7 cm^3/mol) is between that of EC (110.7 cm^3/mol) and DEC (201.2 cm^3/mol). As EC and DEC co-intercalate into PProDOT, this might cause the slightly smaller swelling volume of the polymer in the EC/DEC electrolyte.

Figure 8c shows the diffusion coefficients of the organic solvents, PF_6^-, and Li^+. At the charge neutral state (0%), the diffusion coefficients are of the same order of magnitude as reported in pure electrolytes.[80,82] Moreover, the diffusion coefficients of EC and DEC are close due to solvent-solvent interactions, and the diffusion coefficient of Li^+ in EC/DEC is higher than that in PC.[82] Due to the smaller size and stronger solvation affinity of EC relative to PC, the effective radius of Li^+ first solvation shell is smaller in EC/DEC, which favors Li^+ transport.[72] As PProDOT is oxidized (33%), similar trend is observed which was discussed in Figure 6b and Figure 7c. Moreover, the diffusion coefficient of EC appears to decrease more than that of DEC.

Figure 8d presents the RDF and cumulative CNs between Li^+ and Oc in the organic solvents. The inset is the enlarged view of the CNs shaded in light cyan. At the charge neutral state (0%), the intensity of the first peak in RDF follows the order of EC > PC > DEC. Additionally, the CN for the first solvation shell of Li^+ reaches the plateau more quickly in EC than in PC. These

observations collectively suggest a stronger solvation affinity of Li^+ with EC compared to PC as mentioned earlier. The partial charges of Oc in EC, PC, and DEC are -0.454 *e*, -0.437 *e*, and -0.540 *e*, respectively, providing a justification of the solvation affinity. Moreover, if 4 Å is taken as the effective radius of the first solvation shell, the CN between Li^+ and PC, EC, and DEC is 4.5, 3.7, and 1.0, respectively. This finding is consistent with previous studies on pure electrolytes, where the CN between Li^+ and PC is in the range of 4 to 6, and that between Li^+ and EC/DEC is 3/1.[83–85] Less coordination between Li^+ and DEC stems from the steric hinderance posed by the linear carbonate DEC.[86,87] Upon oxidation of PProDOT (33%), the position of the first peak in RDF remains unchanged, but the intensity diminishes. Concurrently, the CN between Li^+ and PC and EC decreases to 3.5 and 3.4, respectively. The decrease is due to the mass exchange of PC and EC into PProDOT at the expense of their coordination with Li^+. The CN between Li^+ and DEC remains about the same, because of the abundance of free DEC in the electrolyte. As we have seen the marginal increase of the CN between DEC and PProDOT upon oxidation in Figure 8b, this observation is also due to the substantial presence of DEC around PProDOT at the pristine state (0%). Figure S10 demonstrates the RDF and cumulative CNs between PF_6^- and PProDOT, showing the mass transport of anions into PProDOT. The RDF and cumulative CNs between Li^+ and PF_6^- are presented in Figure S11. At the pristine charge neutral state (0%), the RDF and CN are larger in the PC solvent compared to the EC/DEC case. As discussed in Figure 8d where EC shows a stronger solvation affinity, it leaves less coordination of Li^+ with PF_6^- for contact ion pairs. This result is in line with the previous observations.

Dependence on the anion: Finally, we explore the effects of the anion on the mechanical swelling of the polymer, where PProDOT is immersed in the electrolytes of 1.0 M $LiBF_4$, $LiClO_4$, $LiPF_6$, and LiTFSI in PC. Figure S12 shows the final equilibrated states of PProDOT at the

oxidized state (33%) in the four electrolytes. Figure 9a summarizes the modeling results in parallel with the experimental measurements. The swelling volumes are close to those obtained from in-situ nano indentation tests, and the dependence on the anion size is also consistent considering the error bar in experiments. Moreover, the swelling volume of PProDOT in 1.0 M LiTFSI in PC is in great agreement with the value of 30% reported for PProDOT-Hx_2 in the same electrolyte measured by optical ellipsometry.[88] The volume change of PProDOT is roughly proportional to the radius of the anion, following the order of BF_4^- < ClO_4^- < PF_6^- < $TFSI^-$, although an exception is observed in the ClO_4^- case in which the swelling volume is slightly larger than that of PF_6^-. This discrepancy is likely due to the force field parameters. In our modeling, the GAFF compatibility and proper descriptions of the structural and transport properties are the two key factors for the choice of the force field parameters for the electrolytes. Under this consideration, unfortunately, there is no established database encompassing all the needed force field parameters for this work. Therefore, we choose them for the four anions from different literatures as described in the Methodology part. A systematic study of the force field parameterization warrants a separate study and is beyond the scope of this work. The uncertainty of the force field parameters likely causes a slight discrepancy in the cross comparison. Besides, the choice of the reference box within the polymer network can also cause slight variation of the computational results. Nevertheless, our approach and the process in determining the mechanical response of the conducting polymer are well validated by the quantitative comparison with the experimental result and cross checking with literature on the structural characteristics of the polymer, solvation structure in the electrolyte, and the transport properties of the mobile species. The morphological change of PProDOT in the four electrolytes is presented in Figure S13. Figure S13a shows the cumulative CNs between PProDOT atoms at the oxidized state (33%). The curves are nearly overlapping, consistent with the

comparable swelling volumes of PProDOT in the four electrolytes. Seen from the enlarged view of the CNs in the inset, the CN reduces when mechanical swelling becomes larger. Similarly, the XRD patterns (Figure S13b) and the differential CN profiles (Figure S13c) are all comparable at the oxidized state, showing a similar mechanical response of PProDOT in the electrolytes of four different anions. This observation is also consistent with the previous discussion on the swelling mechanism, where the mass transport of the electrolyte and particularly the organic solvent plays a predominant role. Since the organic solvent is identical in the four electrolytes, the variation of the swelling volume of PProDOT is insignificant and mainly comes from the absorption of anions of different sizes. The contribution of $TFSI^-$ is more pronounced compared to other anions because of its large size. As shown in Figure S14a, the CN between $TFSI^-$ and PProDOT is the largest, while the CN between PC and PProDOT with 1.0 M LiTFSI in PC becomes the smallest. The plots demonstrate that anions and the solvent contribute differently to the volume change of the polymer in the four electrolytes. The MD snapshots in the inset of Figure 9a further show the visualization of the absorbed mobile species in the PProDOT network.

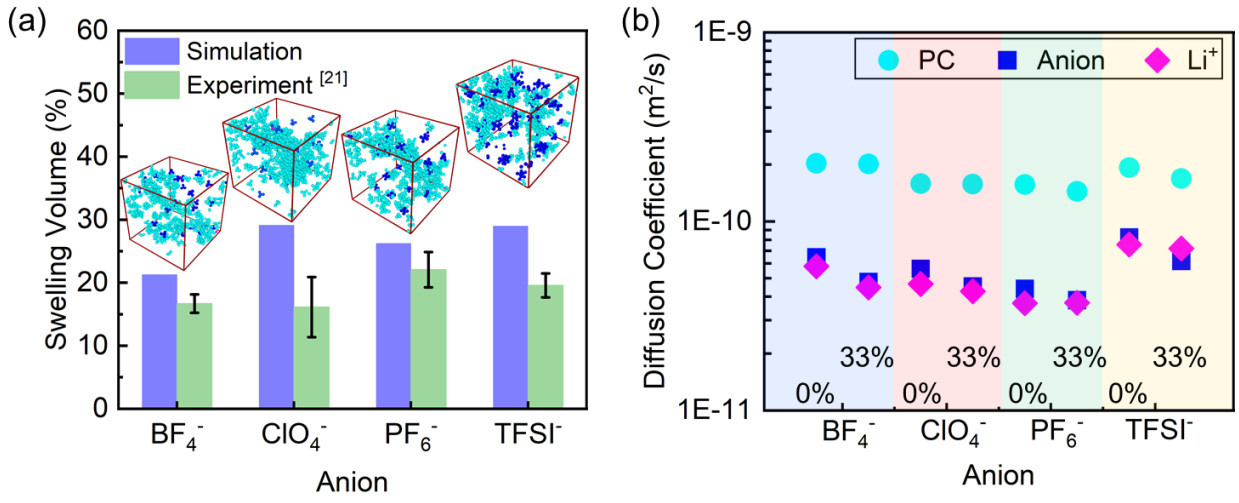

Figure 9. Effects of the anion. (a) Comparison of the swelling volumes of PProDOT with 1.0 M $LiBF_4$, $LiClO_4$, $LiPF_6$, and LiTFSI in PC. Inset figures show the absorbed electrolyte, including the anion (blue), Li^+ (magenta), and PC (cyan) in the reference box of PProDOT where the swelling volume is determined.

(b) Diffusion coefficients of Li^+, PC, and the anion in the four electrolytes when PProDOT is at the charge neutral (0%) and oxidized states (33%).

The solvation structure analysis is included in Figure S15. At the charge neutral state (0%), the first peaks in the RDF between Li^+ and Oc in PC are located at the same position, and the corresponding CNs are 3.2, 3.5, 4.6, and 4.2 in the electrolytes of $LiBF_4$, $LiClO_4$, $LiPF_6$, and LiTFSI, respectively. In the RDF between Li^+ and anions (F in BF_4^-, O in ClO_4^-, F in PF_6^-, and O in $TFSI^-$, Figure S15b), the first peak position follows the order of $BF_4^- < ClO_4^- < PF_6^- \cong TFSI^-$, with nearly equivalent CNs in the first three electrolytes but a lower value in the LiTFSI case. Prior studies on pure electrolytes compared the solvation structures between 1.0 M $LiBF_4$ and $LiPF_6$ in PC.[80] It was found that the first peak in the RDF between Li^+ and Oc in PC were at the same position, but the CN between Li^+ and Oc in PC for the $LiPF_6$ electrolyte showed a larger number (3.72) compared to $LiBF_4$ case (2.66). Meanwhile, the interaction between Li^+ and PF_6^- was weaker than that between Li^+ and BF_4^-. In other words, the first peak location of the RDF between Li^+ and the anion was larger in the $LiPF_6$ electrolyte. Our simulation results are consistent with the previous reports in the pure electrolytes. For the intermediate size of ClO_4^- between BF_4^- and PF_6^-, the interaction between Li^+ and Oc in PC as well as anion would fall in between. A prior DFT study showed more negative binding energy between Li^+ and $TFSI^-$ than that between Li^+ and PF_6^- in the EC solvent, implying a stronger interaction between Li^+ and the anion in the LiTFSI electrolyte.[89] This result is different from our finding. The difference might stem from the scaling (scaling factor of 0.8) of partial charges of $TFSI^-$ and Li^+ for better description of their transport properties in the LiTFSI electrolyte.[44] This scaling factor also explains the larger diffusion coefficients of the LiTFSI electrolyte as shown in Figure 9b. After PProDOT is oxidized (33%), the CNs between Li^+ and Oc in PC reduce to 2.55, 2.91, 3.56, and 4.03 in the electrolytes of $LiBF_4$, $LiClO_4$, $LiPF_6$, and LiTFSI, respectively. Meanwhile, the CN between Li^+ and anions increases in

the first three electrolytes but decreases in the LiTFSI case, which also indicates significant absorption of $TFSI^-$ into the polymer network and its contribution to the mechanical swelling.

Lastly, Figure 9b summarizes the diffusion coefficients of the four electrolytes. There is a tendency for the diffusion coefficients of Li^+ and anions to converge due to the formation of contact ion pairs as discussed before.

Conclusions

In summary, this work presents an extensive study on the molecular mechanism of mechanical swelling of conducting polymers in various liquid electrolyte environments. The swelling volumes are quantitatively determined, and further understood through the detailed analysis on the structural characteristics of the polymer network, the solvation structure in the electrolyte, and the transport properties of the mobile species when the polymer is at different oxidation states. Through calibration of the model systems, we conclude that the mechanical swelling of PProDOT is primarily contributed by the mass transport of the liquid electrolyte and particularly by the absorption of the organic solvent. We then focus on the effects of the electrolytes on the mechanical response of conducting polymers by changing the salt concentration, organic solvent, and anion. Larger deformation of PProDOT is found in the dilute electrolyte as a result of the abundance of the solvent. The mechanical swelling also shows a positive correlation with the size of anions. Through the plots of the RDFs and CNs, the dynamics of the neighboring environment between the polymer chains, anions, cation, and solvents is revealed in detail when the polymer transits from the pristine charge neutral state to the oxidized state. In addition, we find that the diffusion coefficients of the cation, anions, and solvents decrease marginally upon oxidation of the polymer due to the open structure of PProDOT, while the

diffusion coefficients of Li^+ and anions tend to converge due to the formation of contact ion pairs. This theoretical modeling provides fundamental understanding on the molecular motifs behind the mechanical breathing of organic mixed conductors and offer useful guideline in the design of the electrolyte in regulating the mechanical response of conducting polymers in many applications.

Supporting Information. Additional simulation results, including morphological characterizations, solvation structures, and transport properties are included in the Supporting Information.

Acknowledgements

We acknowledge the support by the National Science Foundation through the grants CMMI-1941323 and CMMI-2210158. We are also grateful for the helpful discussions with Prof. Jianguo Mei at Purdue University. We appreciate the discussion and suggestion from Dr. Xiaokang Wang, Dr. Yanbin Wang, Dr. Nikhil Sharma, Jiaxiu Han, and Sameep Rajubhai Shah at Purdue University.

References

(1) Beaujuge, P. M.; Reynolds, J. R. Color Control in π-Conjugated Organic Polymers for Use in Electrochromic Devices. *Chem. Rev.* **2010**, *110* (1), 268–320. DOI: 10.1021/cr900129a

(2) Ke, Z.; Abtahi, A.; Hwang, J.; Chen, K.; Chaudhary, J.; Song, I.; Perera, K.; You, L.; Baustert, K. N.; Graham, K. R.; Mei, J. Highly Conductive and Solution-Processable n-Doped Transparent Organic Conductor. *J. Am. Chem. Soc.* **2023**, *145* (6), 3706–3715. DOI: 10.1021/jacs.2c13051

(3) Perera, K.; Wu, W.; You, L.; Elman, J. F.; Wang, Z.; Wang, X.; Ahmed, M.; Ke, Z.; Mei, J. Absorption Coefficient and Optical Contrast Modulation through Side Chain Engineering of Electrochromic Polymers. *Macromolecules* **2023**, *56* (2), 480–489. DOI: 10.1021/acs.macromol.2c02028

(4) Kukhta, N. A.; Marks, A.; Luscombe, C. K. Molecular Design Strategies toward Improvement of Charge Injection and Ionic Conduction in Organic Mixed Ionic–Electronic Conductors for Organic Electrochemical Transistors. *Chem. Rev.* **2022**, *122* (4), 4325–4355. DOI: 10.1021/acs.chemrev.1c00266

(5) Nielsen, C. B.; Giovannitti, A.; Sbircea, D.-T.; Bandiello, E.; Niazi, M. R.; Hanifi, D. A.; Sessolo, M.; Amassian, A.; Malliaras, G. G.; Rivnay, J.; McCulloch, I. Molecular Design of Semiconducting Polymers for High-Performance Organic Electrochemical Transistors. *J. Am. Chem. Soc.* **2016**, *138* (32), 10252–10259. DOI: 10.1021/jacs.6b05280

(6) Tropp, J.; Meli, D.; Rivnay, J. Organic Mixed Conductors for Electrochemical Transistors. *Matter* **2023**, *6* (10), 3132–3164. DOI: 10.1016/j.matt.2023.05.001

(7) Moia, D.; Giovannitti, A.; A. Szumska, A.; P. Maria, I.; Rezasoltani, E.; Sachs, M.; Schnurr, M.; F. Barnes, P. R.; McCulloch, I.; Nelson, J. Design and Evaluation of Conjugated Polymers with Polar Side Chains as Electrode Materials for Electrochemical Energy Storage in Aqueous Electrolytes. *Energy Environ. Sci.* **2019**, *12* (4), 1349–1357. DOI: 10.1039/C8EE03518K

(8) Paulsen, B. D.; Tybrandt, K.; Stavrinidou, E.; Rivnay, J. Organic Mixed Ionic–Electronic Conductors. *Nat. Mater.* **2020**, *19* (1), 13–26. DOI: 10.1038/s41563-019-0435-z

(9) Marks, A.; Griggs, S.; Gasparini, N.; Moser, M. Organic Electrochemical Transistors: An Emerging Technology for Biosensing. *Adv. Mater. Interfaces* **2022**, *9* (6), 2102039. DOI: 10.1002/admi.202102039

(10) Zhang, Y.; van Doremaele, E. R. W.; Ye, G.; Stevens, T.; Song, J.; Chiechi, R. C.; van de Burgt, Y. Adaptive Biosensing and Neuromorphic Classification Based on an Ambipolar Organic Mixed Ionic–Electronic Conductor. *Adv. Mater.* **2022**, *34* (20), 2200393. DOI: 10.1002/adma.202200393

(11) Gladisch, J.; Stavrinidou, E.; Ghosh, S.; Giovannitti, A.; Moser, M.; Zozoulenko, I.; McCulloch, I.; Berggren, M. Reversible Electronic Solid–Gel Switching of a Conjugated Polymer. *Adv. Sci.* **2020**, *7* (2), 1901144. DOI: 10.1002/advs.201901144

(12) Moser, M.; Gladisch, J.; Ghosh, S.; Hidalgo, T. C.; Ponder Jr., J. F.; Sheelamanthula, R.; Thiburce, Q.; Gasparini, N.; Wadsworth, A.; Salleo, A.; Inal, S.; Berggren, M.; Zozoulenko, I.; Stavrinidou, E.; McCulloch, I. Controlling Electrochemically Induced Volume Changes in Conjugated Polymers by Chemical Design: From Theory to Devices. *Adv. Funct. Mater.* **2021**, *31* (26), 2100723. DOI: 10.1002/adfm.202100723

(13) He, Y.; A. Kukhta, N.; Marks, A.; K. Luscombe, C. The Effect of Side Chain Engineering on Conjugated Polymers in Organic Electrochemical Transistors for Bioelectronic Applications. *J. Mater. Chem. C* **2022**, *10* (7), 2314–2332. DOI: 10.1039/D1TC05229B

(14) Zhao, Y.; Zhao, X.; Zang, Y.; Di, C.; Diao, Y.; Mei, J. Conjugation-Break Spacers in Semiconducting Polymers: Impact on Polymer Processability and Charge Transport Properties. *Macromolecules* **2015**, *48* (7), 2048–2053. DOI: 10.1021/acs.macromol.5b00194

(15) Jensen, J.; Krebs, F. C. From the Bottom Up – Flexible Solid State Electrochromic Devices. *Adv. Mater.* **2014**, *26* (42), 7231–7234. DOI: 10.1002/adma.201402771

(16) Delavari, N.; Gladisch, J.; Petsagkourakis, I.; Liu, X.; Modarresi, M.; Fahlman, M.; Stavrinidou, E.; Linares, M.; Zozoulenko, I. Water Intake and Ion Exchange in PEDOT:Tos Films upon Cyclic Voltammetry: Experimental and Molecular Dynamics Investigation. *Macromolecules* **2021**, *54* (13), 6552–6562. DOI: 10.1021/acs.macromol.1c00723

(17) Wu, R.; Matta, M.; Paulsen, B. D.; Rivnay, J. Operando Characterization of Organic Mixed Ionic/Electronic Conducting Materials. *Chem. Rev.* **2022**, *122* (4), 4493–4551. DOI: 10.1021/acs.chemrev.1c00597

(18) Wu, R.; Paulsen, B. D.; Ma, Q.; Rivnay, J. Mass and Charge Transport Kinetics in an Organic Mixed Ionic–Electronic Conductor. *Chem. Mater.* **2022**, *34* (21), 9699–9710. DOI: 10.1021/acs.chemmater.2c02476

(19) Zozoulenko, I.; Franco-Gonzalez, J. F.; Gueskine, V.; Mehandzhiyski, A.; Modarresi, M.; Rolland, N.; Tybrandt, K. Electronic, Optical, Morphological, Transport, and Electrochemical Properties of PEDOT: A Theoretical Perspective. *Macromolecules* **2021**, *54* (13), 5915–5934. DOI: 10.1021/acs.macromol.1c00444

(20) Wang, X.; Chen, K.; de Vasconcelos, L. S.; He, J.; Shin, Y. C.; Mei, J.; Zhao, K. Mechanical Breathing in Organic Electrochromics. *Nat. Commun.* **2020**, *11* (1), 211. DOI: 10.1038/s41467-019-14047-8

(21) Wang, X.; de Vasconcelos, L. S.; Chen, K.; Perera, K.; Mei, J.; Zhao, K. In Situ Measurement of Breathing Strain and Mechanical Degradation in Organic Electrochromic Polymers. *ACS Appl. Mater. Interfaces* **2020**, *12* (45), 50889–50895. DOI: 10.1021/acsami.0c15390

(22) Hara, S.; Zama, T.; Takashima, W.; Kaneto, K. Artificial Muscles Based on Polypyrrole Actuators with Large Strain and Stress Induced Electrically. *Polym. J.* **2004**, *36* (2), 151–161. DOI: 10.1295/polymj.36.151

(23) Smela, E. Conjugated Polymer Actuators for Biomedical Applications. *Adv. Mater.* **2003**, *15* (6), 481–494. DOI: 10.1002/adma.200390113

(24) Okuzaki, H.; Takagi, S.; Hishiki, F.; Tanigawa, R. Ionic Liquid/Polyurethane/PEDOT:PSS Composites for Electro-Active Polymer Actuators. *Sens. Actuators B Chem.* **2014**, *194*, 59–63. DOI: 10.1016/j.snb.2013.12.059

(25) Wei, B.; Liu, J.; Ouyang, L.; Kuo, C.-C.; Martin, D. C. Significant Enhancement of PEDOT Thin Film Adhesion to Inorganic Solid Substrates with EDOT-Acid. *ACS Appl. Mater. Interfaces* **2015**, *7* (28), 15388–15394. DOI: 10.1021/acsami.5b03350

(26) Momodu, D. Y.; Tong, T.; Zebaze Kana, M. G.; Chioh, A. V.; Soboyejo, W. O. Adhesion and Degradation of Organic and Hybrid Organic-Inorganic Light-Emitting Devices. *J. Appl. Phys.* **2014**, *115* (8), 084504. DOI: 10.1063/1.4867051

(27) Paulsen, B. D.; Giovannitti, A.; Wu, R.; Strzalka, J.; Zhang, Q.; Rivnay, J.; Takacs, C. J. Electrochemistry of Thin Films with In Situ/Operando Grazing Incidence X-Ray Scattering: Bypassing Electrolyte Scattering for High Fidelity Time Resolved Studies. *Small* **2021**, *17* (42), 2103213. DOI: 10.1002/smll.202103213

(28) Savva, A.; Cendra, C.; Giugni, A.; Torre, B.; Surgailis, J.; Ohayon, D.; Giovannitti, A.; McCulloch, I.; Di Fabrizio, E.; Salleo, A.; Rivnay, J.; Inal, S. Influence of Water on the Performance of Organic Electrochemical Transistors. *Chem. Mater.* **2019**, *31* (3), 927–937. DOI: 10.1021/acs.chemmater.8b04335

(29) Tropp, J.; Meli, D.; Wu, R.; Xu, B.; Hunt, S. B.; Azoulay, J. D.; Paulsen, B. D.; Rivnay, J. Revealing the Impact of Molecular Weight on Mixed Conduction in Glycolated Polythiophenes through Electrolyte Choice. *ACS Mater. Lett.* **2023**, *5* (5), 1367–1375. DOI: 10.1021/acsmaterialslett.2c01114

(30) Flagg, L. Q.; Bischak, C. G.; Onorato, J. W.; Rashid, R. B.; Luscombe, C. K.; Ginger, D. S. Polymer Crystallinity Controls Water Uptake in Glycol Side-Chain Polymer Organic Electrochemical Transistors. *J. Am. Chem. Soc.* **2019**, *141* (10), 4345–4354. DOI: 10.1021/jacs.8b12640

(31) Matta, M.; Wu, R.; Paulsen, B. D.; Petty, A. J. I.; Sheelamanthula, R.; McCulloch, I.; Schatz, G. C.; Rivnay, J. Ion Coordination and Chelation in a Glycolated Polymer Semiconductor: Molecular Dynamics and X-Ray Fluorescence Study. *Chem. Mater.* **2020**, *32* (17), 7301–7308. DOI: 10.1021/acs.chemmater.0c01984

(32) Mei, J.; Bao, Z. Side Chain Engineering in Solution-Processable Conjugated Polymers. *Chem. Mater.* **2014**, *26* (1), 604–615. DOI: 10.1021/cm4020805

(33) Flagg, L. Q.; Asselta, L. E.; D'Antona, N.; Nicolini, T.; Stingelin, N.; Onorato, J. W.; Luscombe, C. K.; Li, R.; Richter, L. J. In Situ Studies of the Swelling by an Electrolyte in Electrochemical Doping of Ethylene Glycol-Substituted Polythiophene. *ACS Appl. Mater. Interfaces* **2022**, *14* (25), 29052–29060. DOI: 10.1021/acsami.2c06169

(34) Siemons, N.; Pearce, D.; Cendra, C.; Yu, H.; Tuladhar, S. M.; Hallani, R. K.; Sheelamanthula, R.; LeCroy, G. S.; Siemons, L.; White, A. J. P.; McCulloch, I.; Salleo, A.; Frost, J. M.; Giovannitti, A.; Nelson, J. Impact of Side-Chain Hydrophilicity on Packing, Swelling, and Ion Interactions in Oxy-Bithiophene Semiconductors. *Adv. Mater.* **2022**, *34* (39), 2204258. DOI: 10.1002/adma.202204258

(35) Cendra, C.; Giovannitti, A.; Savva, A.; Venkatraman, V.; McCulloch, I.; Salleo, A.; Inal, S.; Rivnay, J. Role of the Anion on the Transport and Structure of Organic Mixed Conductors. *Adv. Funct. Mater.* **2019**, *29* (5), 1807034. DOI: 10.1002/adfm.201807034

(36) Wang, J.; Wolf, R. M.; Caldwell, J. W.; Kollman, P. A.; Case, D. A. Development and Testing of a General Amber Force Field. *J. Comput. Chem.* **2004**, *25* (9), 1157–1174. DOI: 10.1002/jcc.20035

(37) Franco-Gonzalez, J. F.; Zozoulenko, I. V. Molecular Dynamics Study of Morphology of Doped PEDOT: From Solution to Dry Phase. *J. Phys. Chem. B* **2017**, *121* (16), 4299–4307. DOI: 10.1021/acs.jpcb.7b01510

(38) Kim, D.; Franco-Gonzalez, J. F.; Zozoulenko, I. How Long Are Polymer Chains in Poly(3,4-Ethylenedioxythiophene):Tosylate Films? An Insight from Molecular Dynamics Simulations. *J. Phys. Chem. B* **2021**, *125* (36), 10324–10334. DOI: 10.1021/acs.jpcb.1c04079

(39) Frisch, M. J.; Trucks, G. W.; Schlegel, H. B.; Scuseria, G. E.; Robb, M. A.; Cheeseman, J. R.; Barone, V.; Petersson, G. A.; Nakatsuji, H.; Li, X.; Caricato, M.; Marenich, A. V.; Bloino, J.; Janesko, B. G.; Gomperts, R.; Mennucci, B.; Hratchian, H. P.; Ortiz, J. V.; Izmaylov, A. F.; Sonnenberg, J. L.; Williams-Young, D.; Ding, F.; Lipparini, F.; Egidi, F.; Goings, J.; Peng, B.; Petrone, A.; Henderson, T.; Ranasinghe, D.; Zakrzewski, V. G.; Gao, J.; Rega, N.; Zheng, G.; Liang, W.; Hada, M.; Ehara, M.; Toyota, K.; Fukuda, R.; Hasegawa, J.; Ishida, M.; Nakajima, T.; Honda, Y.; Kitao, O.; Nakai, H.; Vreven, T.; Throssell, K.; Montgomery, J. A., Jr.; Peralta, J. E.; Ogliaro, F.; Bearpark, M. J.; Heyd, J. J.; Brothers, E. N.; Kudin, K. N.; Staroverov, V. N.; Keith, T. A.; Kobayashi, R.; Normand, J.; Raghavachari, K.; Rendell, A. P.; Burant, J. C.; Iyengar, S. S.; Tomasi, J.; Cossi, M.; Millam, J. M.; Klene, M.; Adamo, C.; Cammi, R.; Ochterski, J. W.; Martin, R. L.; Morokuma, K.; Farkas, O.; Foresman, J. B.; Fox, D. J. *Gaussian16, Revision B.01* Gaussian Inc. Wallingford CT, 2016.

(40) Singh, U. C.; Kollman, P. A. An Approach to Computing Electrostatic Charges for Molecules. *J. Comput. Chem.* **1984**, *5* (2), 129–145. DOI: 10.1002/jcc.540050204

(41) Zozoulenko, I.; Singh, A.; Singh, S. K.; Gueskine, V.; Crispin, X.; Berggren, M. Polarons, Bipolarons, And Absorption Spectroscopy of PEDOT. *ACS Appl. Polym. Mater.* **2019**, *1* (1), 83–94. DOI: 10.1021/acsapm.8b00061

(42) Liu, Z.; Huang, S.; Wang, W. A Refined Force Field for Molecular Simulation of Imidazolium-Based Ionic Liquids. *J. Phys. Chem. B* **2004**, *108* (34), 12978–12989. DOI: 10.1021/jp048369o

(43) Baaden, M.; Berny, F.; Madic, C.; Wipff, G. M3+ Lanthanide Cation Solvation by Acetonitrile: The Role of Cation Size, Counterions, and Polarization Effects Investigated by

Molecular Dynamics and Quantum Mechanical Simulations. *J. Phys. Chem. A* **2000**, *104* (32), 7659–7671. DOI: 10.1021/jp001352v

(44) Liu, H.; Maginn, E.; Visser, A. E.; Bridges, N. J.; Fox, E. B. Thermal and Transport Properties of Six Ionic Liquids: An Experimental and Molecular Dynamics Study. *Ind. Eng. Chem. Res.* **2012**, *51* (21), 7242–7254. DOI: 10.1021/ie300222a

(45) Takenaka, N.; Suzuki, Y.; Sakai, H.; Nagaoka, M. On Electrolyte-Dependent Formation of Solid Electrolyte Interphase Film in Lithium-Ion Batteries: Strong Sensitivity to Small Structural Difference of Electrolyte Molecules. *J. Phys. Chem. C* **2014**, *118* (20), 10874–10882. DOI: 10.1021/jp5018696

(46) Martínez, L.; Andrade, R.; Birgin, E. G.; Martínez, J. M. PACKMOL: A package for building initial configurations for molecular dynamics simulations. *J. Comput. Chem.* **2009**, *30* (13), 2157–2164. DOI: 10.1002/jcc.21224

(47) Thompson, A. P.; Aktulga, H. M.; Berger, R.; Bolintineanu, D. S.; Brown, W. M.; Crozier, P. S.; in 't Veld, P. J.; Kohlmeyer, A.; Moore, S. G.; Nguyen, T. D.; Shan, R.; Stevens, M. J.; Tranchida, J.; Trott, C.; Plimpton, S. J. LAMMPS - a Flexible Simulation Tool for Particle-Based Materials Modeling at the Atomic, Meso, and Continuum Scales. *Comput. Phys. Commun.* **2022**, *271*, 108171. DOI: 10.1016/j.cpc.2021.108171

(48) Wang, J.; Wang, W.; Kollman, P. A.; Case, D. A. Automatic Atom Type and Bond Type Perception in Molecular Mechanical Calculations. *J. Mol. Graph. Model.* **2006**, *25* (2), 247–260. DOI: 10.1016/j.jmgm.2005.12.005

(49) Padua, A. fftool, 2013. https://github.com/paduagroup/fftool

(50) Hockney, R. W.; Eastwood, J. W. *Computer Simulation Using Particles*; CRC Press, 2021.

(51) Stukowski, A. Visualization and Analysis of Atomistic Simulation Data with OVITO–the Open Visualization Tool. *Model. Simul. Mater. Sci. Eng.* **2010**, *18* (1), 015012. DOI: 10.1088/0965-0393/18/1/015012

(52) Heck, J.; Goding, J.; Portillo Lara, R.; Green, R. The Influence of Physicochemical Properties on the Processibility of Conducting Polymers: A Bioelectronics Perspective. *Acta Biomater.* **2022**, *139*, 259–279. DOI: 10.1016/j.actbio.2021.05.052

(53) Root, S. E.; Jackson, N. E.; Savagatrup, S.; Arya, G.; Lipomi, D. J. Modelling the Morphology and Thermomechanical Behaviour of Low-Bandgap Conjugated Polymers and Bulk Heterojunction Films. *Energy Environ. Sci.* **2017**, *10* (2), 558–569. DOI: 10.1039/C6EE03456J

(54) Kim, D.; Zozoulenko, I. Why Is Pristine PEDOT Oxidized to 33%? A Density Functional Theory Study of Oxidative Polymerization Mechanism. *J. Phys. Chem. B* **2019**, *123* (24), 5160–5167. DOI: 10.1021/acs.jpcb.9b01745

(55) Kirchmeyer, S.; Reuter, K. Scientific Importance, Properties and Growing Applications of Poly(3,4-Ethylenedioxythiophene). *J. Mater. Chem.* **2005**, *15* (21), 2077. DOI: 10.1039/b417803n

(56) Gueye, M. N.; Carella, A.; Faure-Vincent, J.; Demadrille, R.; Simonato, J.-P. Progress in Understanding Structure and Transport Properties of PEDOT-Based Materials: A Critical Review. *Prog. Mater. Sci.* **2020**, *108*, 100616. DOI: 10.1016/j.pmatsci.2019.100616

(57) Pittelli, S. L.; Keersmaecker, M. D.; Jr, J. F. P.; Österholm, A. M.; Ochieng, M. A.; Reynolds, J. R. Structural Effects on the Charge Transport Properties of Chemically and Electrochemically Doped Dioxythiophene Polymers. *J. Mater. Chem. C* **2020**, *8* (2), 683–693. DOI: 10.1039/C9TC05697A

(58) Bragg, W. L. The Diffraction of Short Electromagnetic Waves by a Crystal. *Scientia* **1929**, *23* (45), 153.

(59) Rudd, S.; Franco-Gonzalez, J. F.; Kumar Singh, S.; Ullah Khan, Z.; Crispin, X.; Andreasen, J. W.; Zozoulenko, I.; Evans, D. Charge Transport and Structure in Semimetallic Polymers. *J. Polym. Sci. Part B Polym. Phys.* **2018**, *56* (1), 97–104. DOI: 10.1002/polb.24530

(60) Makki, H.; Troisi, A. Morphology of Conducting Polymer Blends at the Interface of Conducting and Insulating Phases: Insight from PEDOT:PSS Atomistic Simulations. *J. Mater. Chem. C* **2022**, *10* (42), 16126–16137. DOI: 10.1039/D2TC03158B

(61) Gueye, M. N.; Carella, A.; Massonnet, N.; Yvenou, E.; Brenet, S.; Faure-Vincent, J.; Pouget, S.; Rieutord, F.; Okuno, H.; Benayad, A.; Demadrille, R.; Simonato, J.-P. Structure and Dopant Engineering in PEDOT Thin Films: Practical Tools for a Dramatic Conductivity Enhancement. *Chem. Mater.* **2016**, *28* (10), 3462–3468. DOI: 10.1021/acs.chemmater.6b01035

(62) Moser, M.; Savagian, L. R.; Savva, A.; Matta, M.; Ponder, J. F. Jr.; Hidalgo, T. C.; Ohayon, D.; Hallani, R.; Reisjalali, M.; Troisi, A.; Wadsworth, A.; Reynolds, J. R.; Inal, S.; McCulloch, I. Ethylene Glycol-Based Side Chain Length Engineering in Polythiophenes and Its Impact on Organic Electrochemical Transistor Performance. *Chem. Mater.* **2020**, *32* (15), 6618–6628. DOI: 10.1021/acs.chemmater.0c02041

(63) Gaupp, C. L.; Welsh, D. M.; Reynolds, J. R. Poly(ProDOT-Et2): A High-Contrast, High-Coloration Efficiency Electrochromic Polymer. *Macromol. Rapid Commun.* **2002**, *23* (15), 885–889. DOI: 10.1002/1521-3927(20021001)23:15<885::AID-MARC885>3.0.CO;2-X

(64) Franco-Gonzalez, J. F.; Rolland, N.; Zozoulenko, I. V. Substrate-Dependent Morphology and Its Effect on Electrical Mobility of Doped Poly(3,4-Ethylenedioxythiophene) (PEDOT) Thin Films. *ACS Appl. Mater. Interfaces* **2018**, *10* (34), 29115–29126. DOI: 10.1021/acsami.8b08774

(65) Ongari, D.; Boyd, P. G.; Barthel, S.; Witman, M.; Haranczyk, M.; Smit, B. Accurate Characterization of the Pore Volume in Microporous Crystalline Materials. *Langmuir* **2017**, *33* (51), 14529–14538. DOI: 10.1021/acs.langmuir.7b01682

(66) Einstein, A. On the Movement of Small Particles Suspended in Stationary Liquids Required by the Molecular-Kinetic Theory of Heat. *Annalen der Physik* **1905**, *17*, 549-560.

(67) Nishikawa, K.; Fukunaka, Y.; Sakka, T.; Ogata, Y. H.; Selman, J. R. Measurement of LiClO4 Diffusion Coefficient in Propylene Carbonate by Moiré Pattern. *J. Electrochem. Soc.* **2006**, *153* (5), A830. DOI: 10.1149/1.2178648

(68) Beverina, L.; Pagani, G. A.; Sassi, M. Multichromophoric Electrochromic Polymers: Colour Tuning of Conjugated Polymers through the Side Chain Functionalization Approach. *Chem. Commun.* **2014**, *50* (41), 5413–5430. DOI: 10.1039/C4CC00163J

(69) Fou, A. C.; Rubner, M. F. Molecular-Level Processing of Conjugated Polymers. 2. Layer-by-Layer Manipulation of In-Situ Polymerized p-Type Doped Conducting Polymers. *Macromolecules* **1995**, *28* (21), 7115–7120. DOI: 10.1021/ma00125a013

(70) Xie, J.; Gu, P.; Zhang, Q. Nanostructured Conjugated Polymers: Toward High-Performance Organic Electrodes for Rechargeable Batteries. *ACS Energy Lett.* **2017**, *2* (9), 1985–1996. DOI: 10.1021/acsenergylett.7b00494

(71) Kartha, T. R.; Mallik, B. S. Revisiting LiClO4 as an Electrolyte for Li-Ion Battery: Effect of Aggregation Behavior on Ion-Pairing Dynamics and Conductance. *J. Mol. Liq.* **2020**, *302*, 112536. DOI: 10.1016/j.molliq.2020.112536

(72) Li, T.; Balbuena, P. B. Theoretical Studies of Lithium Perchlorate in Ethylene Carbonate, Propylene Carbonate, and Their Mixtures. *J. Electrochem. Soc.* **1999**, *146* (10), 3613. DOI: 10.1149/1.1392523

(73) Kumar, N.; Seminario, J. M. Lithium-Ion Model Behavior in an Ethylene Carbonate Electrolyte Using Molecular Dynamics. *J. Phys. Chem. C* **2016**, *120* (30), 16322–16332. DOI: 10.1021/acs.jpcc.6b03709

(74) Borodin, O.; Olguin, M.; Ganesh, P.; Kent, P. R. C.; Allen, J. L.; Henderson, W. A. Competitive Lithium Solvation of Linear and Cyclic Carbonates from Quantum Chemistry. *Phys. Chem. Chem. Phys.* **2016**, *18* (1), 164–175. DOI: 10.1039/C5CP05121E

(75) Ganesh, P.; Jiang, D.; Kent, P. R. C. Accurate Static and Dynamic Properties of Liquid Electrolytes for Li-Ion Batteries from Ab Initio Molecular Dynamics. *J. Phys. Chem. B* **2011**, *115* (12), 3085–3090. DOI: 10.1021/jp2003529

(76) Ponrouch, A.; Marchante, E.; Courty, M.; Tarascon, J.-M.; Palacín, M. R. In Search of an Optimized Electrolyte for Na-Ion Batteries. *Energy Environ. Sci.* **2012**, *5* (9), 8572–8583. DOI: 10.1039/C2EE22258B

(77) Xu, K. Nonaqueous Liquid Electrolytes for Lithium-Based Rechargeable Batteries. *Chem. Rev.* **2004**, *104* (10), 4303–4418. DOI: 10.1021/cr030203g

(78) Seo, D. M.; Reininger, S.; Kutcher, M.; Redmond, K.; Euler, W. B.; Lucht, B. L. Role of Mixed Solvation and Ion Pairing in the Solution Structure of Lithium Ion Battery Electrolytes. *J. Phys. Chem. C* **2015**, *119* (25), 14038–14046. DOI: 10.1021/acs.jpcc.5b03694

(79) Ravikumar, B.; Mynam, M.; Rai, B. Effect of Salt Concentration on Properties of Lithium Ion Battery Electrolytes: A Molecular Dynamics Study. *J. Phys. Chem. C* **2018**, *122* (15), 8173–8181. DOI: 10.1021/acs.jpcc.8b02072

(80) Takeuchi, M.; Kameda, Y.; Umebayashi, Y.; Ogawa, S.; Sonoda, T.; Ishiguro, S.; Fujita, M.; Sano, M. Ion–Ion Interactions of LiPF6 and LiBF4 in Propylene Carbonate Solutions. *J. Mol. Liq.* **2009**, *148* (2), 99–108. DOI: 10.1016/j.molliq.2009.07.003

(81) Wu, X.; Ma, L.; Liu, J.; Zhao, K.; Wood, D. L.; Du, Z. Understanding the Effect of Salt Concentrations on Fast Charging Performance of Li-Ion Cells. *J. Power Sources* **2022**, *545*, 231863. DOI: 10.1016/j.jpowsour.2022.231863

(82) Hayamizu, K. Temperature Dependence of Self-Diffusion Coefficients of Ions and Solvents in Ethylene Carbonate, Propylene Carbonate, and Diethyl Carbonate Single Solutions and Ethylene Carbonate + Diethyl Carbonate Binary Solutions of LiPF6 Studied by NMR. *J. Chem. Eng. Data* **2012**, *57* (7), 2012–2017. DOI: 10.1021/je3003089

(83) Borodin, O.; Smith, G. D. Quantum Chemistry and Molecular Dynamics Simulation Study of Dimethyl Carbonate: Ethylene Carbonate Electrolytes Doped with LiPF6. *J. Phys. Chem. B* **2009**, *113* (6), 1763–1776. DOI: 10.1021/jp809614h

(84) Saitoh, K.; Takai, Y.; Sato, T.; Takuma, M.; Takahashi, Y. Optimization of LIB Electrolyte and Exploration of Novel Compounds via the Molecular Dynamics Method. *Batteries* **2022**, *8* (3), 27. DOI: 10.3390/batteries8030027

(85) Skarmoutsos, I.; Ponnuchamy, V.; Vetere, V.; Mossa, S. Li+ Solvation in Pure, Binary, and Ternary Mixtures of Organic Carbonate Electrolytes. *J. Phys. Chem. C* **2015**, *119* (9), 4502–4515. DOI: 10.1021/jp511132c

(86) Su, C.-C.; He, M.; Amine, R.; Chen, Z.; Yu, Z.; Rojas, T.; Cheng, L.; Ngo, A. T.; Amine, K. Unveiling Decaying Mechanism through Quantitative Structure-Activity Relationship in Electrolytes for Lithium-Ion Batteries. *Nano Energy* **2021**, *83*, 105843. DOI: 10.1016/j.nanoen.2021.105843

(87) Tian, Z.; Zou, Y.; Liu, G.; Wang, Y.; Yin, J.; Ming, J.; Alshareef, H. N. Electrolyte Solvation Structure Design for Sodium Ion Batteries. *Adv. Sci.* **2022**, *9* (22), 2201207. DOI: 10.1002/advs.202201207

(88) Das, P.; Zayat, B.; Wei, Q.; Salamat, C. Z.; Magdău, I.-B.; Elizalde-Segovia, R.; Rawlings, D.; Lee, D.; Pace, G.; Irshad, A.; Ye, L.; Schmitt, A.; Segalman, R. A.; Miller, T. F. I.; Tolbert, S. H.; Dunn, B. S.; Narayan, S. R.; Thompson, B. C. Dihexyl-Substituted Poly(3,4-Propylenedioxythiophene) as a Dual Ionic and Electronic Conductive Cathode Binder for Lithium-Ion Batteries. *Chem. Mater.* **2020**, *32* (21), 9176–9189. DOI: 10.1021/acs.chemmater.0c02601

(89) Chen, X.; Zhang, X.; Li, H.; Zhang, Q. Cation−Solvent, Cation−Anion, and Solvent−Solvent Interactions with Electrolyte Solvation in Lithium Batteries. *Batter. Supercaps* **2019**, *2* (2), 128–131. DOI: 10.1002/batt.201800118